AGU PUBLICATIONS

Journal of Advances in Modeling Earth Systems

RESEARCH ARTICLE
10.1002/2015MS000427

Key Points:
- Interactive PSC/stratospheric sulfate model embedded in CESM
- Nonequilibrium growth of Type Ib PSC particles
- Homogeneous nucleation of Type Ia PSC particles

Correspondence to:
Y. Zhu,
yunqian.zhu@colorado.edu

Citation:
Zhu, Y., O. B. Toon, A. Lambert, D. E. Kinnison, M. Brakebusch, C. G. Bardeen, M. J. Mills, and J. M. English (2015), Development of a Polar Stratospheric Cloud Model within the Community Earth System Model using constraints on Type I PSCs from the 2010–2011 Arctic winter, *J. Adv. Model. Earth Syst.*, *7*, 551–585, doi:10.1002/2015MS000427.

Received 6 JAN 2015
Accepted 25 MAR 2015
Accepted article online 31 MAR 2015
Published online 18 APR 2015

Development of a Polar Stratospheric Cloud Model within the Community Earth System Model using constraints on Type I PSCs from the 2010–2011 Arctic winter

Yunqian Zhu[1], Owen B. Toon[1], Alyn Lambert[2], Douglas E. Kinnison[3], Matthias Brakebusch[1,4], Charles G. Bardeen[3], Michael J. Mills[3], and Jason M. English[1]

[1]Department of Atmospheric and Oceanic Sciences, Laboratory for Atmospheric and Space Physics, University of Colorado, Boulder, Colorado, USA, [2]Jet Propulsion Laboratory, California Institute of Technology, Pasadena, California, USA, [3]National Center for Atmospheric Research, Boulder, Colorado, USA, [4]Now at Department of Environmental Science and Analytical Chemistry, Stockholm University, Stockholm, Sweden

Abstract Polar stratospheric clouds (PSCs) are critical elements of Arctic and Antarctic ozone depletion. We establish a PSC microphysics model using coupled chemistry, climate, and microphysics models driven by specific dynamics. We explore the microphysical formation and evolution of STS (Supercooled Ternary Solution) and NAT (Nitric Acid Trihydrate). Characteristics of STS particles dominated by thermodynamics compare well with observations. For example, the mass of STS is close to the thermodynamic equilibrium assumption when the particle surface area is >4 $\mu m^2/cm^3$. We derive a new nucleation rate equation for NAT based on observed denitrification in the 2010–2011 Arctic winter. The homogeneous nucleation scheme leads to supermicron NAT particles as observed. We also find that as the number density of NAT particles increases, the denitrification also increases. Simulations of the PSC lidar backscatter, denitrification, and gas phase species are generally within error bars of the observations. However, the simulations are very sensitive to temperature, which limits our ability to fully constrain some parameters (e.g., denitrification, ozone amount) based on observations.

1. Introduction

Polar stratospheric clouds (PSCs) form in the lower stratosphere during the polar night. Thermal radiation to space combined with a lack of solar heating in wintertime cools the winter polar stratosphere, while the strong winds in the polar vortex isolate the cold polar air from the warm air at lower latitudes. During the winter of 2010–2011, a cold Arctic vortex lasted from December until the end of March [*Manney et al.*, 2011; *Sinnhuber et al.*, 2011]. The unusual length of this cold period resulted in a prolonged presence of PSCs and significant gradual denitrification. The denitrification provides a useful test for modeling Nitric Acid Trihydrate (NAT) formation. Here we develop and test a new 3-D model of PSCs using data from the 2010–2011 Arctic winter. This model could potentially make improved forecasts for PSC formation and ozone depletion, though the sensitivity of the results to temperature may make forecasts challenging in the Arctic.

PSCs are important to understand because heterogeneous reactions on PSCs convert inactive chlorine ($ClONO_2$ and HCl) into photochemically active chlorine [*Solomon et al.*, 1986], which together with related reactions involving Br causes extensive ozone loss when sunlight is available to drive catalytic cycles [*Molina and Molina*, 1987]. PSCs also denitrify, reducing NO_y, and thereby slowing the reformation of chlorine and bromine reservoirs [*Toon et al.*, 1986]. In addition, falling ice-PSC particles dehydrate the winter polar vortex, mainly over Antarctica [*Kelly et al.*, 1989], and perhaps a larger part of the Southern Hemisphere stratosphere [*Schoeberl and Dessler*, 2011]. Observed cooler Arctic stratospheres in recent years, coupled with more severe ozone depletion, increase the need to improve the modeling of PSCs [*Rieder et al.*, 2014].

The efficiency of chlorine and bromine activation, denitrification, and dehydration varies between the multiple types of PSCs and stratospheric sulfates. Observations show that the microphysics and the heterogeneous chemical influences of PSCs are quite complicated. Recent research indicates that chlorine activation is due more to the presence of supercooled ternary solution (STS) rather than to nitric acid trihydrate (NAT) particles [*Kühl et al.*, 2004; *Wegner et al.*, 2012]. Some studies suggest that cold sulfates are also very

important because measurements show enhanced ClO and decreased HCl at temperatures below 195 K even in the absence of significant polar stratospheric cloud particle surface area [*Hanson et al*., 1994; *Kawa et al*., 1997; *Drdla and Müller*, 2012; *Wegner et al*., 2012]. Ice clouds also provide surface area for heterogeneous chemistry, but reactions on other PSC types are fast enough that the chemistry has often gone to completion before it has become cold enough for significant amounts of ice clouds to form [*Wegner et al*., 2013]. Observations and theories suggest that large NAT particles with small number densities, rather than ice particles, are the predominant cause of denitrification [*Toon et al*., 1990; *Waibel et al*., 1999; *Fahey et al*., 2001; *Lambert et al*., 2012].

PSCs are classified into two main categories based upon their chemical and physical properties. Type I PSCs are composed primarily of H_2O and HNO_3 in either a crystalline phase, NAT (or Type Ia), or a liquid phase, supercooled ternary solutions, STS (or Type Ib). Type II PSCs, on the other hand, consist of crystalline water-ice particles (which probably contain small amounts of nitric acid and sulfuric acid) [*Toon et al*., 1989; *Lowe and MacKenzie*, 2008].

As the main particles found in the stratosphere outside the polar vortex, liquid H_2SO_4 aerosols serve as the condensation centers for HNO_3 and H_2O when STS particles form in the winter season in both hemispheres. NAT particles are solids, and their formation requires a phase change. The processes that form NAT are still not clear, but are likely to be of three main types. One possible type of process is that H_2SO_4 aerosols freeze to form sulfuric acid tetrahydrate (SAT). Then through nucleation followed by condensation of nitric acid, SAT becomes coated by NAT. However, this process is unlikely, because SAT deliquesces to form STS as nitric acid supersaturations rise due to falling temperatures [*Koop and Carslaw*, 1996]. A second possible process is heterogeneous freezing of nitric acid to form NAT on ice [*Middlebrook et al*., 1996; *Biermann et al*., 1998; *Carslaw et al*., 1998; *Waibel et al*., 1999; *Wirth et al*., 1999]. NAT is likely left behind when the ice sublimes, a process that has been observed directly in wave clouds [*Peter et al*., 1994; *Wirth et al*., 1999]. Another possibility is that Type Ib STS particles may freeze, either heterogeneously [*Hoyle et al*., 2013] or homogeneously [*Carslaw et al*., 2002; *Tabazadeh et al*., 2002; *Daerden et al*., 2007], to form NAT (possibly with nitric acid dihydrate (NAD) as an intermediate phase [*Bertram et al*., 1996; *Disselkamp et al*., 1996; *Bertram and Sloan*, 1998]). The existence of homogeneous nucleation of NAT from STS in the stratosphere is under debate. As we will show the nucleation rates involved are very small, and hence difficult to observe in laboratory settings. Some studies suggested that the NAT could homogeneously nucleate from STS if stratospheric temperature remains near 190 K for more than 1 day [*Salcedo et al*., 2000]. However, bulk experiments [*Koop et al*., 1995, 1997, 2000] suggest that liquid stratospheric aerosol droplets exist without freezing for temperatures higher than the ice frost point unless the H_2SO_4 weight percent is below 0.01%. Some measurements [*Curtius et al*., 2005; *Murphy et al*., 2007; *Weigel et al*., 2014] report that nonvolatile residuals are found inside the PSC particles, which indicates the possibility of heterogeneous nucleation of NAT by micrometeorites. While each of these processes may occur in the polar vortex over broad geographic regions, it is also possible that NAT formation is heavily influenced by stratospheric mountain waves. The waves can introduce small spatial scale, but large amplitude, temperature fluctuations which may promote the freezing of STS directly to NAT [*Tsias et al*., 1997; *Zondlo et al*., 2000]. At very low temperatures, Type II PSCs composed of ice form by freezing Type Ib PSCs [*Toon et al*., 1989; *Tabazadeh et al*., 1994]. Ice particles can also form through heterogeneous nucleation from STS containing insoluble nuclei [*Engel et al*., 2013] or SAT [*Fortin et al*., 2003].

The goal of this study is to investigate the formation of Type I PSCs, the dominant PSC clouds in the Arctic region during the winter of 2010–2011. In this work, we answer three questions:

1. Can our model properly simulate the particle volume, size distribution, lidar backscatter, PSC composition, and other data related to the fundamental properties of the clouds that are important for ozone loss?
2. Can our model properly simulate the denitrification during the Arctic winter 2010–2011?
3. Can our model properly simulate the evolution of ozone and the related chemicals controlling ozone over the 2010–2011 Arctic winter?

Below we first review the data that are available for the Arctic winter of 2010–2011 and for other years that might be relevant. We next discuss the model we use to simulate the PSCs. We then present comparisons of simulations with the data, and address the three questions posed above.

2. Observational Databases for PSCs

2.1. CALIPSO

The CALIOP (Cloud-Aerosol Lidar with Orthogonal Polarization) lidar system onboard the CALIPSO (Cloud-Aerosol Lidar and Infrared Pathfinder Satellite Observations) spacecraft has been operating since June 2006 [*Winker et al*., 2007]. CALIOP is a two-wavelength, polarization sensitive lidar. It provides both high vertical resolution profiles (60–180 m for lower stratosphere) of backscatter at 532 and 1064 nm and two orthogonal (parallel and perpendicular) polarization components at 532 nm [*Winker et al*., 2007]. The space-based lidar classification scheme was developed from the ratio of the perpendicular to parallel component of aerosol backscatter $\delta_{aerosol}$, called the depolarization ratio, and the inverse scattering ratio ($1/R_{532}$) [*Pitts et al*., 2009]. The scattering ratio, R_{532}, is the ratio of total volume backscatter at 532 nm to the molecular backscatter coefficient at 532 nm. The detailed classifications of compositions based on these quantities are described by Pitts et al. [*Pitts et al*., 2007, 2011, 2013].

CALIOP not only provides high spatial (smoothed to 5 km horizontal resolution and 180 m vertical resolution for PSC products) and temporal resolution observations of the distribution of PSCs, but also provides considerable insight into PSC composition and formation mechanisms [*Pitts et al*., 2007, 2009, 2011]. By using the PSC identification algorithm and composition classification scheme [*Pitts et al*., 2009], CALIPSO can provide time series of PSC coverage, which together with the altitude profile determines the volume of the winter vortex containing PSCs. The data used in this research are based on version 1 CALIOP Level 2 PSC data products available through the NASA Langley Atmospheric Science Data Center (ASDC) (http://eosweb.larc.nasa.gov/).

2.2. Aura MLS

MLS is the Microwave Limb Sounder onboard NASA's Earth Observing System (EOS) Aura satellite. Aura was launched into a near-polar sun-synchronous orbit in 2004 [*Schoeberl*, 2007], and continues to collect data as of this writing. MLS observes on a global scale both day and night. Aura MLS is based on UARS (Upper Atmosphere Research Satellite) MLS [*Waters et al*., 1999]. MLS measures millimeter and submillimeter wavelength thermal emission, which can avoid the obscuration caused by aerosols or thin clouds in infrared and shorter wavelength observations. Aura MLS is able to measure temperature and many species in the gas phase, and we are interested in the following species in this paper: H_2O, HCl, HNO_3, and O_3. The typical vertical resolution of observations at lower stratosphere is 2–3.7 km for H_2O, ~3 km for HCl, 3–5 km for HNO_3, and 2.5 km for O_3. The MLS systematic error (accuracy) for HNO_3 is $\pm$0.25–0.5 ppbv for 100–32 hPa and $\pm$0.5–1 ppbv for 22 hPa. The random error (precision) is $\pm$0.7 ppbv for MLS HNO_3 data. For the vertical level 20–68 hPa, the MLS accuracy is 4–7% for H_2O, 0.05–0.2 ppmv for O_3, and 0.1–0.2 ppbv for HCl; the precision is 6–8% for H_2O, 0.04–0.1 ppmv for O_3, and 0.2 ppbv for HCl [*Livesey et al*., 2011] (http://mls.jpl.nasa.gov/).

2.3. MIPAS

MIPAS (Michelson Interferometer for Passive Atmospheric Sounding) operated onboard the sun-synchronous polar orbiting Envisat (Europe's Environmental monitoring satellite) from July 2002 to April 2012. Since 2005, the latitudinal coverage of MIPAS tangent points ranges from 87.5°S to 89.3°N at 3.7° latitude steps, and typically from 6 to 70 km altitude in its nominal observation mode. It is a Fourier transform spectrometer taking limb sounding infrared measurements between 685 and 2410 cm^{-1} (14.6–4.15 μm). The spectra can be analyzed to measure pressure, temperature, the concentrations of gas phase species, as well as the abundance of PSCs and their composition over a continuous vertical profile [*Höpfner et al*., 2006; *Fischer et al*., 2008]. Since MIPAS mid-infrared spectra are affected by cloud interferences, cloudy sweeps are removed from the analysis so only a partial coverage of the vortex can be obtained at PSC altitude. In this paper, we make use of data from the MIPAS2D database [*Dinelli et al*., 2010] retrieved with a 2-D tomographic approach and will compare the model results with MIPAS observations of HNO_3 and $ClONO_2$ [*Arnone and Hauchecorne*, 2012; *Arnone et al*., 2012]. The accuracy of HNO_3 measured by MIPAS is 7–13% for the area in which we are interested, and the random error is 2–10% [*Dinelli et al*., 2010; *Arnone et al*., 2012]. For $ClONO_2$ [*Arnone and Hauchecorne*, 2012; *Arnone et al*., 2012] observed by MIPAS, the accuracy is 5–20% and the precision is 2–10% (0.05–0.15 ppbv). The adopted data were self-consistently interpolated to potential temperature levels and averaged within the vortex by *Arnone et al*. [2012].

2.4. ACE-FTS

The Atmospheric Chemistry Experiment (ACE) measures the concentrations of atmospheric constituents by absorption spectroscopy using the sun as a light source [*Bernath*, 2006]. Both PSCs and cirrus clouds can be seen clearly by a high-spectral resolution (0.02 cm^{-1}) Fourier Transform Spectrometer (FTS) from 2 to 13 μm (750–4100 cm^{-1}) and the visible/near IR imagers at 0.527 and 1.020 μm, with a good vertical and horizontal resolution (1 km), during sunset and sunrise [*Dodion et al*., 2007]. The PSC size distributions and volume density for different components of particles can be obtained from the ACE data based on the wavelength dependence of aerosol bands in the spectrum. The retrieval technique is based on a least squares retrieval between a measured spectrum and the reference spectra. For example, the reference spectra of liquid droplets (STS) use the Mie approximation [*Bohren and Huffman*, 1983]; while, the discrete dipole technique [*Draine and Flatau*, 1994] is used for the solid hydrates and ice particles.

2.5. SCIAMACHY (Scanning Imaging Absorption SpectroMeter for Atmospheric CHartographY)

SCIAMACHY (Scanning Imaging Absorption SpectroMeter for Atmospheric CHartographY) onboard ESA's Envisat satellite [*Burrows et al*., 1995; *Bovensmann et al*., 1999] measures the limb scattered solar radiation. Using the radiation profiles from 750 to and 1090 nm, *Von Savigny et al*. [2005] define a threshold to detect PSCs, called the color index ratio. In this paper, we will compare the model results with SCIAMACHY limb data retrieved at PSC altitudes in the 2010–2011 [*Hommel et al*., 2014] Arctic winter.

2.6. In Situ Observations

Unfortunately, we are not aware of any in situ data in the Arctic winter of 2010–2011, so we use data from earlier years. Our rationale for using data from other years is that many, but not all, PSC properties are controlled by equilibrium thermodynamics. These properties should be fixed by temperature, as well as the abundances of H_2O and HNO_3, with little influence from the air mass history. During the Airborne Arctic Stratosphere Experiment (AASE) in January and February 1989, 14 NASA ER-2 flights took measurements of PSCs and sulfate aerosols at potential temperatures of 440–460 K (nominal pressures of 50–60 hPa [*Dye et al*., 1992]) using a forward scattering spectrometer probe (FSSP) model 300 [*Dye et al*., 1990; *Baumgardner et al*., 1992]. These studies provide detailed measurements of PSC particle volume.

On 9 December 2001, a balloon-borne gondola provided detailed in situ measurements of particle composition, size, number concentration, phase, and backscatter in an Arctic stratospheric cloud between 22 and 26 km [*Deshler et al*., 2003a]. On this balloon flight, particle compositions of HNO_3 and H_2O were measured by an aerosol mass spectrometer [*Schreiner et al*., 2002]. The particle size and number concentrations were measured using four optical particle counters [*Deshler and Oltmans*, 1998; *Deshler et al*., 2003b]. Particle phase was derived from depolarization measurements at 532 nm using a laser backscattersonde described by *Adriani et al*. [1999]. Water vapor was measured by a frost point hygrometer [*Ovarlez and Ovarlez*, 1994], and temperature was measured by a Vaisala temperature sensor.

During the SOLVE/THESEO (the Stratospheric Aerosol and Gas Experiment (SAGE) III Ozone Loss and Validation Experiment and the Third European Stratospheric Experiment on Ozone) campaign between January and March in 2000 Arctic winter, the NASA ER-2 high-altitude aircraft with three instruments onboard flew through the lower stratosphere and identified large nitric acid hydrate particles (diameter more than 10 μm) for the first time inside the polar vortex [*Fahey et al*., 2001]. The sizes were retrieved from observations by the NOAA NO_y instrument, which has a front inlet and rear inlet that allow it to distinguish particle diameters less and greater than 2 μm. Later, this discovery was confirmed by direct observations of size distributions using the Multiangle Aerosol Spectrometer Probe (MASP) [*Brooks et al*., 2003]. In the 2009–2010 Arctic winter, large NAT particles were observed again during the RECONCILE (Reconciliation of Essential Process Parameters for an Enhanced Predictability of Arctic Stratospheric Ozone Loss and its Climate Interactions) campaign [*Von Hobe et al*., 2013]. *Molleker et al*. [2014] retrieved the size distribution with sizes between 1 and 40 μm based on the detection of single scattered laser light by the FSSP-100 instrument.

We compare the simulated particle volume with the ER-2 flight observation in 1989. Also, we compare the simulated particle size distribution with the balloon data in 2001, ACE observation, ER-2 flight observation during SOLVE/THESEO campaign in 2000, and M-55 aircraft observation during RECONCILE campaign in 2009–2010.

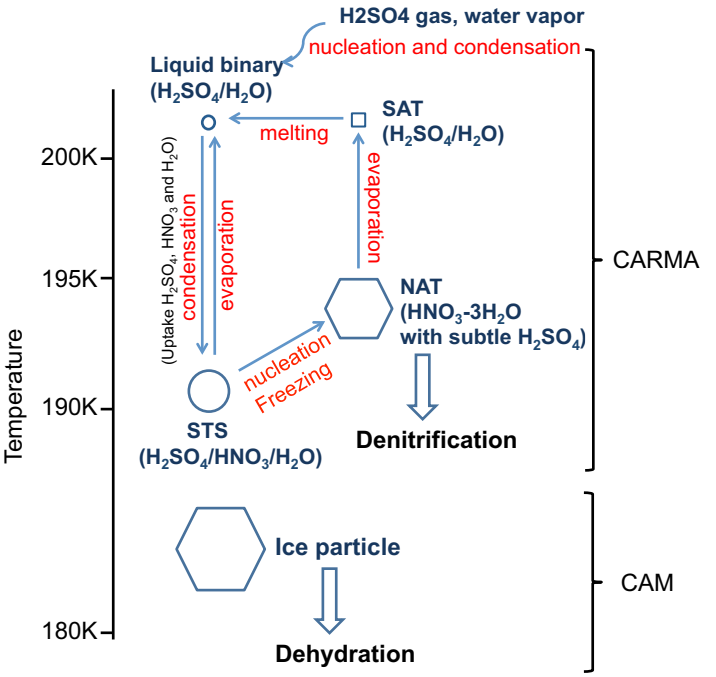

Figure 1. The PSCs formation schemes in our model. The liquid phase particles are symbolized as circles and solid phase particles as square and hexagons. The arrows indicate the main falling particles. CARMA includes the processes that are treated within the CARMA microphysical package; CAM (WACCM) indicates the processes that are using the standard CAM (WACCM) microphysical parameterizations.

3. SD-WACCM/CARMA PSC Model Description

The Community Aerosol and Radiation Model for Atmospheres (CARMA) [*Toon et al.*, 1988] has been coupled with the Whole-Atmosphere Community Climate Model [*Garcia et al.*, 2007] with Specified Dynamics (SD-WACCM-4.0) to simulate the advection, diffusion, sedimentation, deposition, coagulation, nucleation, and condensational growth of atmospheric aerosols [*Bardeen et al.*, 2008]. The NCAR Community Earth System Model (CESM) is the common numerical framework for WACCM [*Marsh et al.*, 2013]. In these simulations, a horizontal resolution of 1.9° in latitude and 2.5° in longitude is used. The model is defined on 88 vertical levels ranging from 6×10^{-6} hPa, roughly 140 km, down to the surface. The vertical resolution is about 1 km in the lower stratosphere. CARMA-3.0 simulates the main microphysical processes and transport due to sedimentation and Brownian diffusion. SD-WACCM transports the aerosols using resolved winds and eddy motions.

The SD-WACCM model uses the MOZART chemical model (the Model for Ozone And Related chemical Tracers) [*Brasseur et al.*, 1998; *Hauglustaine et al.*, 1998; *Horowitz et al.*, 2003; *Kinnison et al.*, 2007; *Emmons et al.*, 2010; *Lamarque et al.*, 2012] to treat the PSC heterogeneous chemical processes. In the current versions of WACCM, STS and NAT form at a prescribed supersaturation with a prescribed size distribution and number density [*Kinnison et al.*, 2007; *Wegner et al.*, 2013]. In our SD-WACCM/CARMA version, we replace the STS and NAT parameterizations with microphysical processes. The time and space varying surface area density and effective radius of PSCs and sulfates derived from CARMA pass into MOZART for heterogeneous reaction rate calculations. The prognostic H_2O routines in WACCM are used to treat ice cloud formation and dehydration [*Wegner et al.*, 2013]. The SD-WACCM/CARMA run is four time slower than a SD-WACCM run because of an additional seven sulfur chemistry tracers and 80 PSC tracers. The sulfur chemistry includes reactions involving OCS, SO, SO_2, S, HSO_3, SO_3, and H_2SO_4 [*English et al.*, 2011, and references therein]. The PSC tracers in the model include 20 size bins each for HNO_3 and H_2SO_4 in STS, as well as 20 bins each for H_2SO_4 (as SAT) and HNO_3 in NAT. Particulate water is not treated explicitly in the aerosol, but rather is assumed to stay in equilibrium with the gas phase.

In addition to PSCs, SD-WACCM/CARMA contains a complete package for stratospheric sulfates [*English et al.*, 2011]. The sulfate model treats particles composed of H_2SO_4 and H_2O and has been compared with observations [*English et al.*, 2011]. We do not currently consider micrometeorites, though other versions of the model have included them [*Neely et al.*, 2011]. HNO_3 has been added to this sulfate model by including the growth of HNO_3 within the sulfate particles for STS and the growth of HNO_3 in NAT. The main microphysical processes for PSCs include homogeneous nucleation of sulfuric acid from the gas phase [*English et al.*, 2011], homogeneous nucleation of NAT from STS, as well as condensation and evaporation of sulfuric and nitric acid. Figure 1 presents the main aerosol types that are involved in PSC microphysical processes in our model. The detailed descriptions of these microphysical processes related

Table 1. The Parameter Settings in the Base Case Model and Other Tuning Values

Parameter	Base Case	Variation
Temperature	GEOS5	−1.5 K [*Brakebusch*, 2013]
CARMA time step	1.7 s to 15 min[a]	
CARMA bins	20 bins for each species	
PSC dry radius range	0.000343–22.26 μm	
Sulfate particle surface area for heterogeneous chemistry	Reduced by 4 at and above 650 K potential temperature	
HNO_3 diffusion coefficient	$D\_HNO_3 = 0.466 D\_H_2O$ (see Appendix A)	
STS particle shape	Sphere	
Growth (liquid) Accommodation coefficient	1.0	
Coagulation Accommodation coefficient	1.0	
Temperature Accommodation coefficient	1.0	
Growth (solid) Accommodation coefficient	0.93	0.4, 0.2 [*Crowley et al.*, 2010]
NAT nucleation scheme	STS scheme (no NAT nucleates)	NATscheme, NAT/J10, NADscheme, NAD/J100, slopeflat[b]
NAT particle density (g/cm^3)	1.62 [*Taesler et al.*, 1975]	0.81
NAT particle shape	Sphere	Flat plate (ratio of length and radius is 0.2)

[a]We constrain the supersaturation change of the species to limit the time step.
[b]The definitions of case names are given in section 3.4.

to PSCs formation are given below. Parameter settings for the base case and for several sensitivity cases are listed in Table 1.

We use the SD-WACCM/CARMA model nudged with Goddard Earth Observing System 5 (GEOS5) [*Reinecker et al.*, 2008] assimilated data every 30 min with a nudging relaxation of time of 50 h [*Brakebusch et al.*, 2013]. The GEOS5 data have a resolution of 6 h and are interpolated into 30 min nudging intervals. From the tests done by *Brakebusch et al.* [2013] and *Brakebusch* [2013], the mean difference between the simulations and GEOS5 data are -0.16 ± 0.77 K for temperature, -0.08 ± 1.83 m/s for zonal wind, and -0.01 ± 1.9 m/s for meridional wind. The model fields that are nudged are: horizontal winds, temperatures, surface pressure, surface wind stress, and sensible and latent surface heat flux. The nudging scheme is applied below 50 km; the model is fully interactive above 60 km. A linear transition is applied between 50 and 60 km. The temperature is a significant factor for PSC heterogeneous chemical reaction rates [*Brakebusch et al.*, 2013] and PSC formation, especially the NAT nucleation rate as shown in section 3.4. Unfortunately, GEOS5 is not reality and the small temperature differences between GEOS5 and reality can be significant as we discuss below.

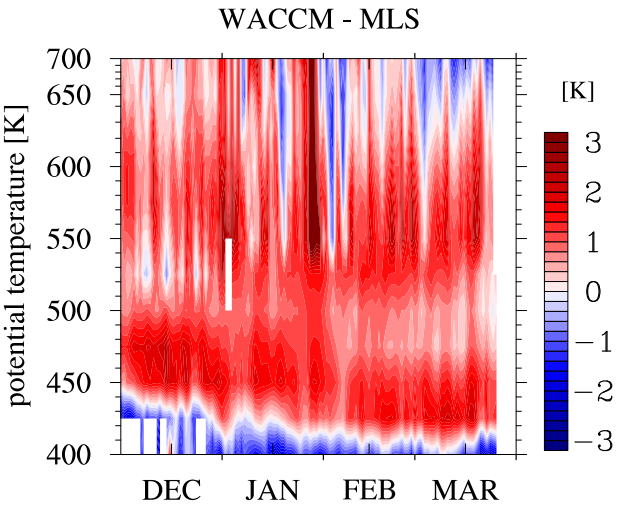

Figure 2. The SD-WACCM temperature minus the MLS temperature at different potential temperatures inside the vortex from 1 December 2010 to 31 March 2011. The blank regions indicate missing values.

Figure 2 shows the temperature difference between MLS temperatures and SD-WACCM [*Brakebusch*, 2013; *Brakebusch*

et al., 2013]. Figure 2 shows that model temperatures are about 1.5° warmer than MLS temperatures from 450 K to 550 K, which is the main PSC formation area in the northern hemisphere. Below this region, model temperatures are about 0.5°–1° colder than the MLS temperatures around 400–450 K. The validation of MLS version 3.3 temperature also states that the differences between GEOS5 and MLS are -0.5 ± 0.3 to $+1.5 \pm 0.6$ K between 100 and 17 hPa at the pole [*Schwartz et al*., 2008; *Livesey et al*., 2011]. The temperature accuracy for MLS data is −2 to 0 K for the region from 17 to 52 hPa and 0–1 K for 52 to 100 hPa. The MLS precision is ±0.6 and ±0.8 K [*Livesey et al*., 2011]. Although the temperature difference is small, as we will show below changes in the temperature in the model by 1 K can lead to significant differences in nucleation rates, which reflect themselves in significant differences in the simulated denitrification.

We initialize using 5 year SD-WACCM runs to stabilize the stratospheric chemistry and sulfate aerosols. We start the simulations on 1 October 2010 before PSCs formed in the Arctic and run until the end of March 2011 when PSCs had disappeared.

3.1. Condensation and Evaporation

Once nucleation of sulfuric acid particles occurs, H_2SO_4 vapor and water vapor condense on these background sulfate aerosols in the stratosphere [*Turco et al*., 1979; *Hamill et al*., 1982]. As the temperature decreases, HNO_3 gas will condense on the sulfate aerosols. This condensation results in STS formation. We do not assume that STS is in equilibrium with nitric acid vapor, as most other PSC models do, but rather follow its growth kinetically. Once NAT nucleates, the NAT particles also grow and evaporate.

The growth and evaporation equation for NAT and STS, discussed in Appendix A, is described in *Toon et al*. [1989] and is similar to that employed by *Barkstrom* [1978] and subsequent work [*Ramaswamy and Detwiler*, 1986]. This equation provides the particle growth/evaporation rate, and hence how much H_2SO_4 and HNO_3 mass should be moved between bins.

The growth equation requires equations for acid concentrations, vapor pressures, and surface tensions among others. The acid concentration, or weight percent, is required to calculate vapor pressure, surface tension, and ternary solution density. The weight percent of HNO_3, H_2SO_4, and H_2O [*Luo et al*., 1995] assumes that water vapor is in equilibrium with the particles, and varies with particle size. The HNO_3 vapor pressure uses the Luo et al. equations for STS [*Luo et al*., 1995] and Hanson's equations for NAT [*Hanson and Mauersberger*, 1988]. The surface tension and particle density of ternary solutions is calculated by using empirical polynomial equations [*Martin et al*., 2000]. The detailed equations are listed in Appendix A.

3.2. Coagulation

As the particles move through the atmosphere, coagulation occurs when the particles collide with each other. The coagulation equations for our model are described in Appendix B. The numerical algorithm is based on *Jacobson et al*. [1994].

Coagulation of PSC particles with each other is not a very important process, because their numbers are small and their lifetimes are short. However, it is essential to consider coagulation for the longer-lived sulfuric acid particles, particularly when active nucleation is occurring. In the stratosphere, once the sulfate particles have grown to sizes near 10 nm or larger, coagulation controls the particle numbers, and the nucleation scheme is of little importance [*English et al*., 2011].

3.3. Vertical Transport

After the particle forms, it will be transported across the spatial grid. WACCM performs the transport by winds and eddy diffusion, and CARMA performs the transport forced by gravity and Brownian diffusion. Brownian diffusion is not important except above 100 km where the atmosphere starts to separate by molecular weight. The fall velocities are computed with the Stokes-Cunningham equation [*Fuks*, 1964], as described in Appendix C.

3.4. NAT Homogeneous Nucleation and SAT Melting

After STS has formed due to the condensational growth, nitric acid trihydrate (NAT) and nitric acid dihydrate (NAD) can crystalize from it though homogeneous nucleation, or possibly through heterogeneous nucleation. Unfortunately, the nucleation processes are not understood at the present time. We explore several possible homogeneous nucleation pathways as discussed below. To calculate how fast STS nucleates into

NAT, we calculate the nucleation probability, which represents the probability that an STS particle will convert into NAT in a certain time period [*Koop et al*., 1997]. *Tabazadeh et al*. [2002] concluded that surface-based nucleation was more consistent than volume-based nucleation with all the available laboratory kinetic data. The nucleation probability based on surface nucleation rate is written as [*Koop et al*., 1997]:

$$Nuc_{probability} = 1 - \exp\left(-J_s \cdot Surface\ \ Area \cdot dt\right) \tag{1}$$

where *dt* is a CARMA time step. For the *Surface Area*, we use the surface area of an individual STS particle in each size bin. The NAT surface-based nucleation rate is written as [*Tabazadeh et al*., 2002]:

$$J_s = N_s \left(\frac{kT}{h}\right) exp[\frac{-\Delta G^s_{act}}{RT}] \tag{2}$$

In this equation, $N_s = X_{HNO3}{}^* n_s$. X_{HNO3} is the mole fraction of HNO_3 on the surface of the particle, and n_s is the approximate number density of molecular surface sites, which is about 10^{15} cm^{-2}. *k* is the Boltzmann constant; *h* is the Planck constant; *R* is the gas constant; *T* is the temperature; and ΔG^s_{act} is the nucleus free energy. We use the following empirical equations for the formation free energy for NAT surface-based nucleation [*Tabazadeh et al*., 2002]:

$$\Delta G^{s,NAD}_{act}(X_{HNO3}, T) = 11.5593 + 0.0804214T - \{71.5133 - 0.256724T\}X_{HNO3} \tag{3}$$

$$\Delta G^{s,NAT}_{act}(X_{HNO3}, T) = (-45.2429 + 0.364844T)\frac{\Delta G^{NAD}_{act}(X_{HNO3}, T)}{\Delta G^{NAD}_{act}(0.246, T)} \tag{4}$$

Figure 3 illustrates the average HNO_3 mole fraction in STS particles as a function of temperature from our model simulation, the nucleus free energy for five test cases and their corresponding nucleation probability. Figure 3a is the average mole fraction we sample in our model at a pressure of 50 hPa at the beginning of the winter before the onset of denitrification and dehydration. The particles take up HNO_3 as the temperature decreases below 200 K and STS starts to form. Eventually, a maximum nitric acid mole fraction is reached around 190 K, and at lower temperatures, the HNO_3 mole fraction declines because the particles take up H_2O quickly as the temperature approaches the frost point. The mole fractions and temperatures are used to compute the nucleus free energy (shown in Figure 3b) and the nucleation probabilities (shown in Figure 3c) using the equations described above or with some modification (see Table 2). The curves shown in the example in Figure 3c are derived assuming a typical STS particle with 0.25 μm radius and surface area of 0.785 μm^2.

We conduct several simulations based on variants of the NAT surface nucleation equation from *Tabazadeh et al*. [2002]. Table 2 shows short names for the various nucleation rate equations used in simulations and the main characteristics of the simulations. First, we use the NAT and NAD surface nucleation equations [*Tabazadeh et al*., 2002]. Then, we divide the nucleation rate, J_s, by 10 and 100, respectively (shown by dashed lines in Figure 3b), which shifts the nucleation probability about 1 and 2 orders of magnitude lower than in the NAT and NAD scheme. Note dividing J by a factor is equivalent to adding a constant to the free energy terms for the unmodified J. The factors are listed in Table 2. Note that the NAT schemes have a very abrupt onset near 190 K, while the NAD schemes have a less sensitive temperature dependence. The case labeled slopeflat was obtained by dividing the nucleation free energy in NAT scheme equation by 2, and then adding a constant, as noted in Table 2.

The nucleation probability of the slopeflat nucleation scheme is less dependent on temperature (and HNO_3 mole fraction) than the other four schemes as shown in Figure 3c. The free energy of the slopeflat case is within 10% of the free energy of the NAD and NAT schemes; it is very close to the NADJ/100 case [*Knopf et al*., 2002; *Voigt et al*., 2005; *Höpfner et al*., 2006] which has been applied in Daerden's model [*Daerden et al*., 2007]. The measurements used to retrieve the equations in Tabazadeh's paper have an order of magnitude uncertainty in the nucleation rate and an uncertainty of about 2° in temperature. Moreover, *Tabazadeh et al*. [2002] had to extrapolate the laboratory data over temperature and over mole fraction. The free energies for five cases shown in Figure 3 are within about 10% of the values from each other, but the J values vary by 6 orders of magnitude. Given the small variations in the free energies in Figure 3, and the extrapolations made in deriving them by *Tabazadeh et al*. [2002], we

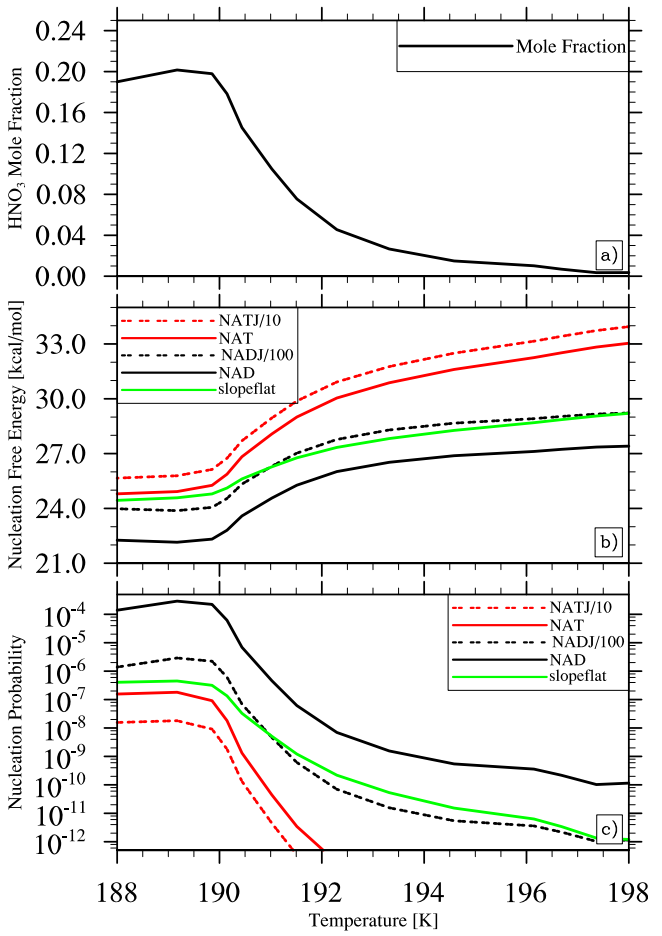

Figure 3. (a) The modeled HNO_3 mole fraction; (b) Calculates the nucleus free energy based on the equations in this section and the HNO_3 mole fraction shown in Figure 3a; (c) The nucleation probability of one typical STS particle in 30 min (one WACCM physics-time step). The names of five cases refer to Table 2.

feel we are justified in varying the free energy slightly to obtain better fits with observed denitrification as discussed below.

The nucleation probability in Figure 3c increases rapidly as temperature declines from 193 to 190 K. However, this perceived dependence on temperature is somewhat misleading. Figure 4 shows that the nucleation free energy is actually very sensitive to the mole fraction of the STS compared with its sensitivity to the temperature. Falling temperatures, however, generally cause the mole fraction to increase. Eventually, the nucleation rate (Figure 3) reaches a plateau as the temperature drops because the mole fraction of HNO_3 in STS starts to decline at very low temperatures.

As discussed below, the 2010–2011 Arctic winter does not provide extensive data for empirically deriving the nucleation rate. Therefore, the equation for slopeflat case may be improved in the future when further years with Arctic denitrification may be observed. Note, however, in Figure 3 that about 1 STS particle in 1 million is converted to a NAT particle in 30 min. The rate, which incidentally makes laboratory measurements very difficult, is consistent with observations. STS particles have a radius that is about 30 times smaller than that of developed NAT particles. Therefore, the mass of 40 NAT particles would be comparable to the mass of the remaining 1 million STS particles (mass is proportional to the cube of NAT radius). Therefore, large NAT particles cannot be very numerous or STS/NAT mixtures would contain little STS. Of course, since most optical observations are sensitive to particle area rather than mass, at the same mass, small STS particles are more effective than large NAT particles at altering optical properties, as discussed by *Toon et al.* [2000], and therefore easier to detect.

Our simulations only produce NAT particles with relatively large sizes. However, there may be other mechanisms, not treated here, that would produce small NAT particles. The nucleation rate of NAT from STS might increase substantially in mountain wave clouds or gravity waves if very low temperatures are accompanied by high mole fractions of nitric acid when STS is driven out of equilibrium due rapid the temperature changes [*Tsias et al.*, 1997]. Also, ice particles in mountain wave clouds are known to be numerous and

Table 2. Summary of Scenarios

Short Name	Descriptions	ΔG Formula
STS only	Only STS particles form	None
NATscheme	NAT surface nucleation scheme	Equations (2) and (4)
NATJ/10	NAT scheme with $J_s/10$	$\Delta G_{act}^{s,NAT}+2.3RT$
Slopeflat	Nucleation probability less dependent on temperature and mole fraction	$(\Delta G_{act}^{s,NAT}+63.45RT)/2$
NADscheme	NAD surface nucleation scheme	Equations (2) and (3)
NADJ/100	NAD scheme with $J_s/100$	$\Delta G_{act}^{s,NAD}+4.6RT$

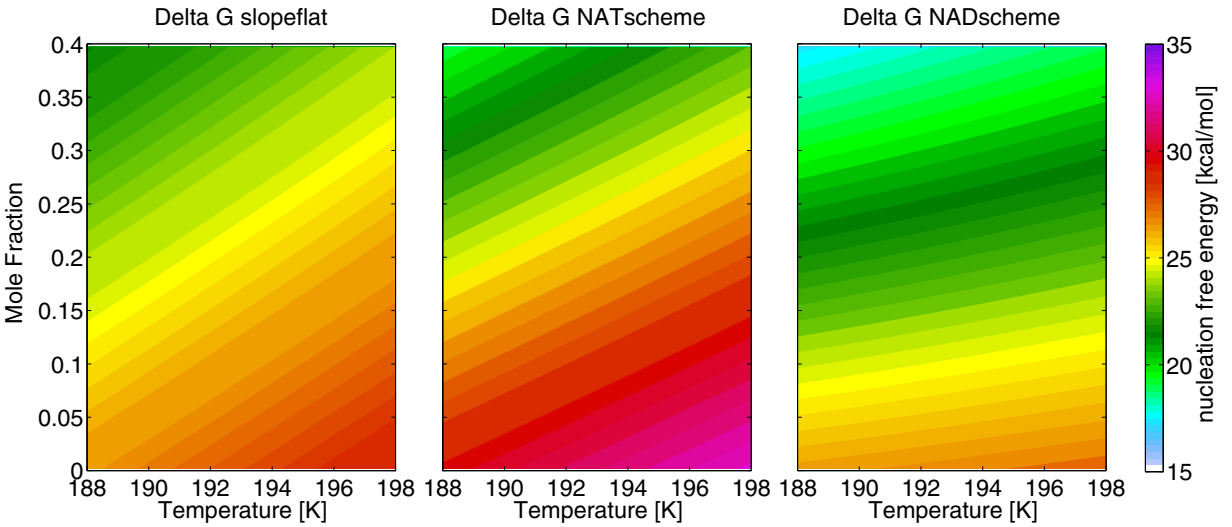

Figure 4. The nucleation free energy (kcal/mol) as a function of mole fraction of HNO_3 inside an STS particle and the temperature for three test cases: slopeflat, NATscheme, and NADscheme.

small. Therefore, NAT formed on ice particles in such waves are likely to have small particle sizes [*Carslaw et al*., 1998; *Luo et al*., 2003].

When the temperature rises, ice and NAT particles evaporate and leave SAT behind. SAT will melt when the temperature is warmer than 210–215 K [*Middlebrook et al*., 1993]. However, SAT also deliquesces if the temperature declines and the NAT supersaturation increases [*Koop and Carslaw*, 1996]. It is also proved by laboratory [*Iraci et al*., 1995] and calculations [*MacKenzie et al*., 1995] that the nucleation from SAT to NAT requires supercooling by up to 8 K. Therefore, if NAT evaporates, our model converts all the SAT particles back into STS, and NAT is not allowed to recondense on them until nucleation of NAT from STS occurs again.

4. SD-WACCM/CARMA Simulations of PSCs

4.1. Microphysical Features of PSCs in the Base Case Model

Before proceeding to a detailed analysis of the PSCs in the 2010–2011 winter, we first present some microphysical results from the base case STS-only model and the slopeflat case. There are certain parts of the model, such as weight percent of species in STS particles and STS particle volumes, that are basically related to thermodynamics, and do not depend on the detailed history of the PSCs, assuming only that the total water vapor and total nitric acid are known. Other parameters such as the STS particle size distribution may depend on the PSC history, but also can be roughly compared with data with similar current environmental conditions due to rapid equilibrium times.

4.1.1. Weight Percent of Species Inside STS Particles

The weight percent of STS particles (equivalent to mole fraction) is very important for NAT nucleation, because the NAT nucleation probability is very sensitive to the HNO_3 mole fraction as shown in Figure 4. Since our model uses nonequilibrium calculations for STS growth, comparing the weight percent computed in the model with equilibrium values indicates how fast STS particles respond to temperature changes. Generally, the weight percent is controlled by thermodynamics, so it is more or less independent of the details of the atmospheric dynamics and the history of the PSCs given fixed abundances of water and nitric acid. The "average weight percent" is the total mass of each composition in a grid box divided by the total mass of STS, so it is effectively a volume-weighted average.

Figure 5 shows the STS particle weight percent from the model at 52 hPa from 1 day of the STS-only case compared with the weight percent from Carslaw's thermodynamic model [*Carslaw et al*., 1995] at the same pressure level. Each circle in Figure 5 represents the average weight percent of different species in one

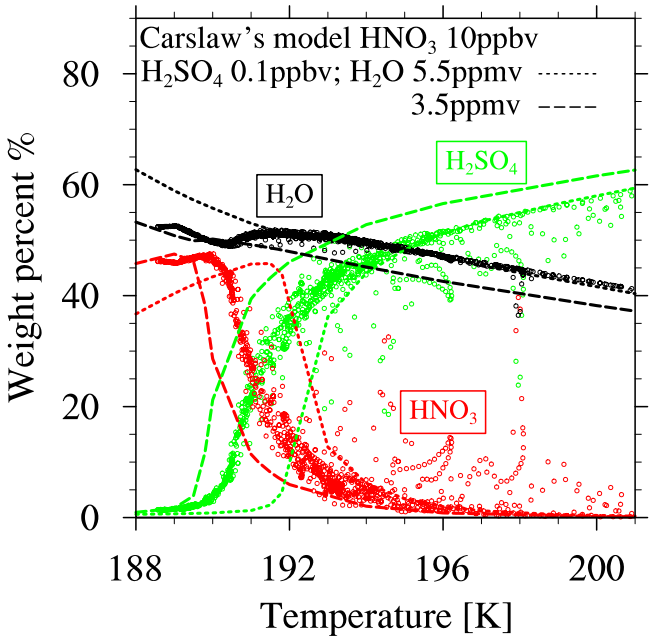

Figure 5. Weight percent of each species in STS particles from the model (colored circles) around 52 hPa compared with Carslaw's model with 3.5 ppm H_2O (dashed lines) and 5.5 ppm H_2O (dotted lines).

model grid box, with particle sizes about 0.05–0.5μm. Note that in our model, the weight percent varies across the size spectrum so that the weight percent of some bins could be different from the weight percent shown in this graph. However, the bins that have the typical STS sizes (0.05–0.25 μm) do not vary significantly from the means in Figure 5, because the mass mostly concentrates in those bin sizes. For Carslaw's model, we assume 10 ppbv HNO_3 and 0.1 ppbv H_2SO_4 and present results for two different water vapor mixing ratios, 3.5 ppmv H_2O and 5.5 ppmv H_2O. These choices for H_2O, HNO_3, and H_2SO_4 are close to the values of these species in the model. The HNO_3 in the model is about 10 ppbv $\pm$ 0.3 ppbv, and H_2SO_4 is about 0.1 ppbv $\pm$ 0.1 ppbv. The H_2O is within 3.5–5.5 ppmv. The model results are in the range of Carslaw's thermodynamic model for temperatures between 188 and 192 K, which means that the STS generally remains close to equilibrium at these temperatures.

Figures 5 and 6 show that at some places the weight percent of HNO_3 and H_2SO_4 are outside the range of equilibrium values at temperatures above about 192 K, where the particles contain little nitric acid. This lack of equilibrium occurs because the sulfate aerosols have small surface area density (around 3 $\mu m^2/cm^3$, shown in Figure 6), which is not enough surface area to pull the ambient nitric acid vapor to equilibrium quickly. Figure 6 indicates that in those regions with surface areas larger than about 4 $\mu m^2/cm^3$, the particles are in equilibrium with the HNO_3 vapor. As illustrated in section 4.2, surface areas are often lower than 4 $\mu m^2/cm^3$, and therefore the use of an equilibrium model for STS will lead to errors in predictions of STS masses, sizes, and acid concentrations.

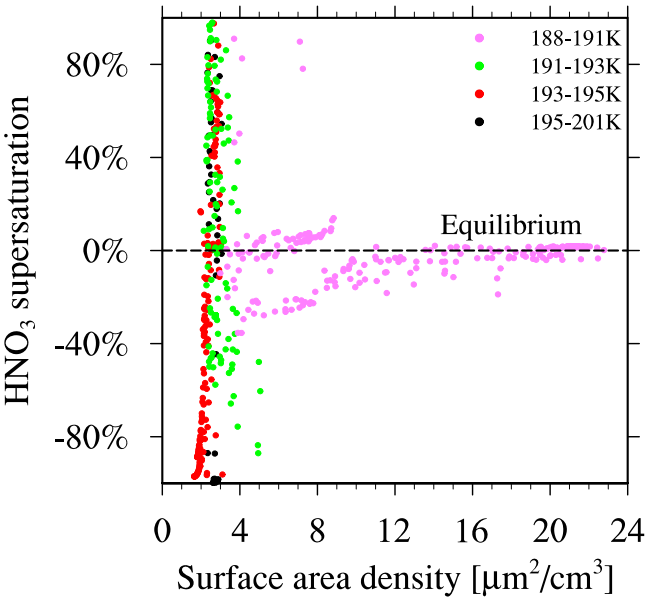

Figure 6. HNO_3 supersaturation with respect to STS as a function of surface area density using the same sample points as Figure 5. Different colors represent the different temperature range. Negative supersaturation means that the particles are evaporating.

4.1.2. Particle Volume

Particle volume represents the amount of the total reservoir of nitric acid that is condensed. Comparing simulated to observed particle volume as a function of temperature is an indirect test of the growth scheme in the model, and a direct test of the thermodynamics. Generally, the particle volume is controlled by thermodynamics, so it is more or less independent of the details of

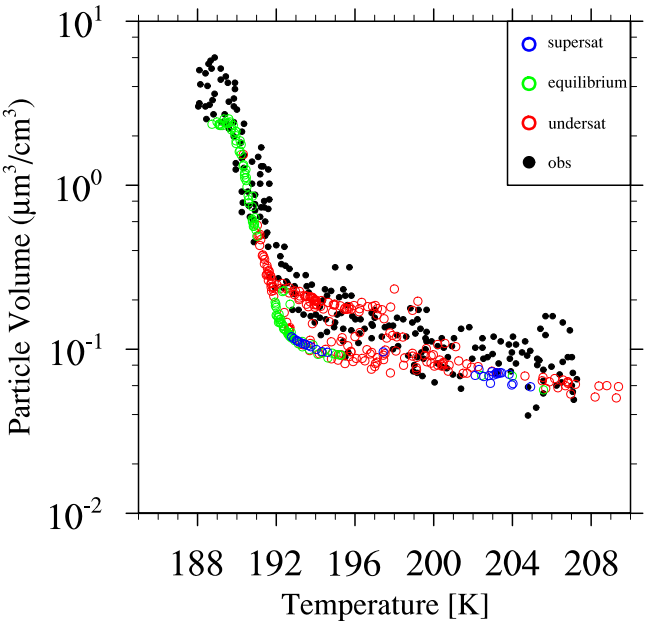

Figure 7. The particle volumes from the STS-only model (colored circles) compared with ER-2 aircraft observations (black dots) in January and February, 1989 at 50–60 hPa [*Dye et al.*, 1992]. The different colors represent different saturation status of HNO_3 over the particles.

the atmospheric dynamics and the history of the PSCs, given fixed abundances of water and nitric acid.

Figure 7 shows the particle volumes from the STS-only model (colored circles) compared with ER-2 aircraft observations (black dots) [*Dye et al.*, 1992]. The different colors for the model represent the supersaturation of HNO_3 over the particles. The blue circles represent the particles with HNO_3 supersaturated, these particles tend to absorb more HNO_3 into the particles. The red circles represent the particles with HNO_3 undersaturated, these particles tend to evaporate HNO_3 into gas phase. The green circles represent the particles with HNO_3 generally in equilibrium. As the temperature decreases, the sulfate particles take up HNO_3 and water to form STS. Once the temperature decreases to 192 K, the particle volume increases rapidly as the HNO_3 vapor pressure over the STS particles falls, and nitric acid and water are moved from the gas phase to the condensed phase. Most of those colder particles are in equilibrium. When the temperature is above 196 K, the particle volume is not highly dependent on the HNO_3 saturation ratio because the main components of the particles are H_2SO_4 and water. When the temperature is above 200 K, the particle volume from the model is slightly lower than the observations. At temperatures between 192 and 196 K, the model shows two values of volume, with one value generally representing undersaturated conditions and the other supersaturated conditions. The differences between the volumes are not only caused by the varying HNO_3 and H_2O spatial distribution in the model, but also occur because the particles with small volumes do not have enough time to reach equilibrium with the vapor because of their low surface area density. At temperatures below 190 K, the model, which only has such low temperatures at relatively low latitudes, has about half the volume observed. However, the gas phase H_2O and HNO_3 were not measured. If we assume an STS number density of 10 cm^{-3}, in order to have the particle volume of 6 $\mu m^3/cm^3$ when the temperature is lower than 190 K as observed, the STS particle size

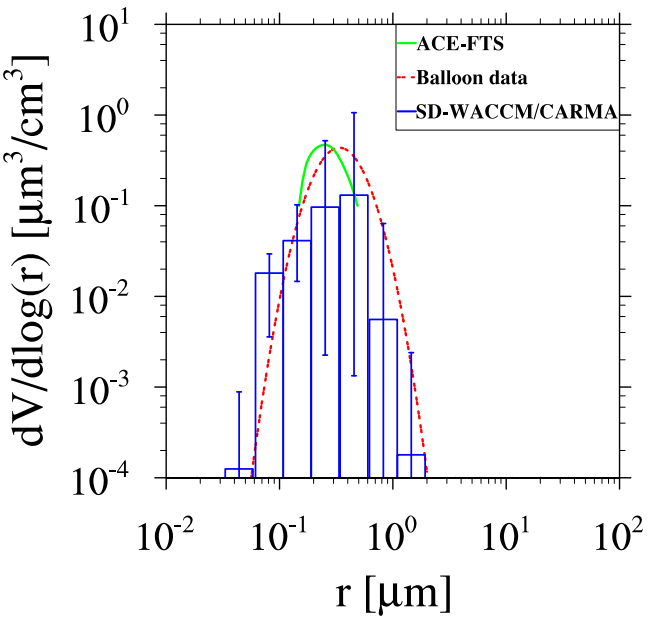

Figure 8. Vortex average volume size distributions from the base case STS-only simulation of SD-WACCM/CARMA (blue) at 18–19 km compared with ACE-FTS data (green) [*Zasetsky et al.*, 2007] at 18–23 km in 2005 and balloon observation (red) [*Deshler et al.*, 2003a] at 22–26 km in 2001.

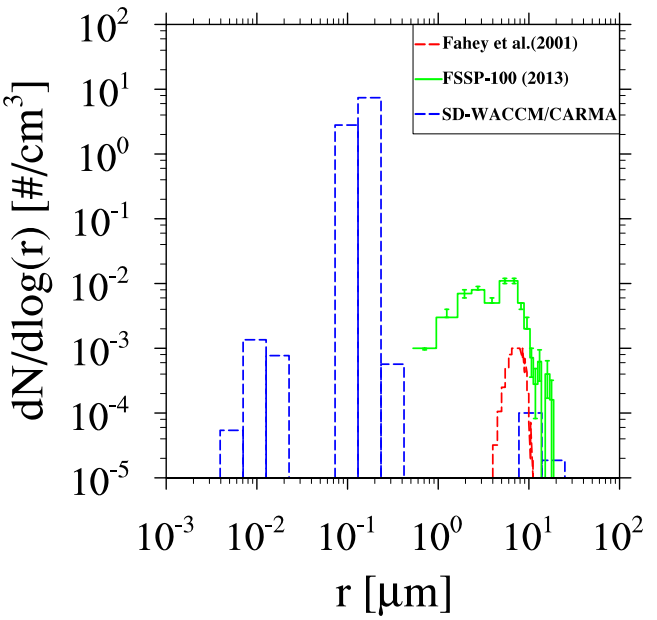

Figure 9. Number size distribution of STS and NAT particles from case slopeflat of SD-WACCM/CARMA (blue) at around 18 km compared with the NOy instrument observations in 1999–2000 [*Fahey et al.*, 2001] and FSSP-100 instrument observations in 2009–2010 [*Molleker et al.*, 2014] around the same height.

would be about 0.5 μm. This size is much bigger than a typical STS particle size (0.05–0.3 μm). Therefore, the observed PSCs must have a significant H_2O uptake to increase the particle size significantly when the temperature is lower than 190 K.

4.1.3. Size Distribution

The particle size distribution may reflect the history of the particles. Sizes vary as condensation or evaporation occurs, which is rapid for STS. However, the NAT portion of the size distribution depends on the number of STS particles that nucleated to form NAT, the amount of time the NAT has had to grow, and can also be affected by particle sedimentation removing particles as they fall, or adding them if they descend from higher layers.

Figure 8 shows the STS simulated volume size distribution at about 18–19 km (52 hPa) averaged over the entire polar vortex on 24 January 2011 in the base case STS-only model, compared with the observations at particular locations in prior years. In the simulation, the total nitric acid averaged over the vortex at this location was about 10 ppbv. The size distribution of STS will shift slightly as the total nitric acid varies.

Figure 9 illustrates a simulated size distribution using the slopeflat nucleation scheme at 71°N–75°N and 102°E–110°E at 61 hPa (~17–18 km) on 2 January 2011 compared with NAT observations in previous years. The size distribution of NAT particles is largely dependent on the air mass history, and highly variable in observations and in our model. This comparison is meant to point out that the homogeneous nucleation

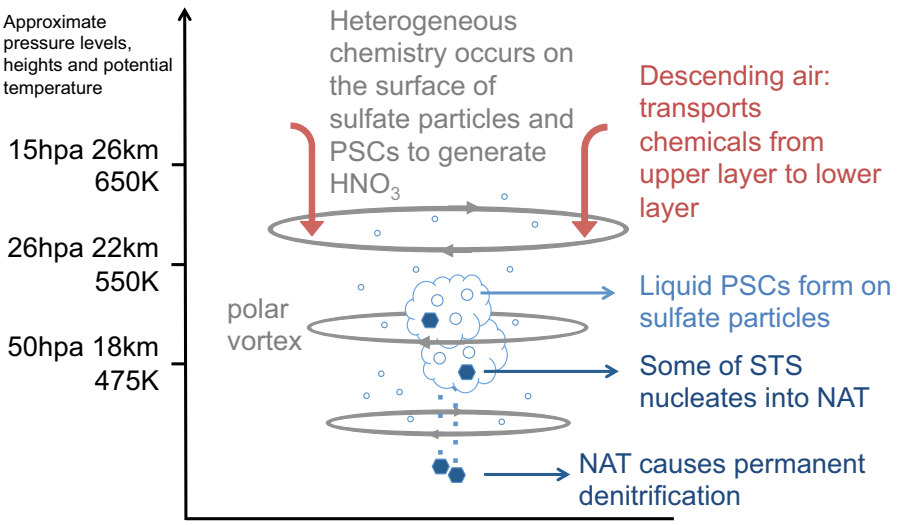

Figure 10. The source and sink terms that influence the HNO_3 abundance in the polar night.

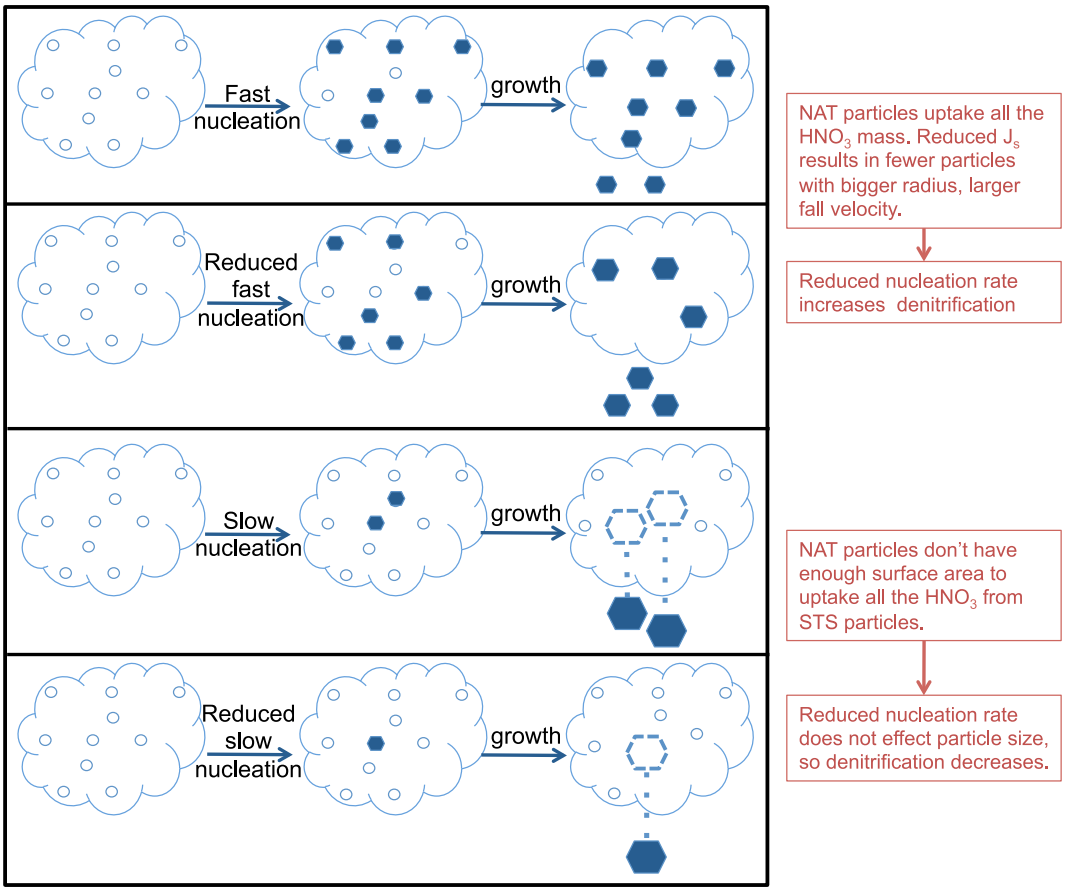

Figure 11. Diagram showing the impacts of nucleation rates on particle size, particle fall velocities, and denitrification.

scheme is able to simulate some of the larger NAT particles that have been observed. The observations are from the FSSP-100 instrument on the M-55 aircraft during the 2009–2010 winter [*Molleker et al.*, 2014] and from the NO_y instrument on ER-2 aircraft in 1999–2000 described by *Fahey et al.* [2001] around the same height. The observations here only show NAT particles while the simulations include both STS and NAT. The simulations produce particles in the same general range of sizes, but the total numbers of particles and shapes of the distributions vary significantly. In part, these differences can be attributed to different histories of the particles in the model and observations, and of course differences in temperatures, and nitric acid abundance between the years of the observations and simulations. They also likely represent different nucleation rates between the model and nature.

4.2. Denitrification During the 2010–2011 Winter

Denitrification is one of the indicators of whether the NAT nucleation scheme is realistic since NAT is the main contributor to denitrification. Figure 10 describes the possible processes that influence the HNO_3 concentration during the polar night inside the polar vortex. These processes include chemistry, transport, and microphysics. Heterogeneous chemistry is a significant source of HNO_3. Reactions on sulfate particles and on PCSs convert $ClONO_2$ and N_2O_5 to HNO_3. Therefore, a proper treatment of sulfate aerosols is very important for HNO_3 prediction. STS takes up HNO_3 but will not cause permanent denitrification (temporary removal from the gas phase does occur) since the fall velocity of STS is very small, so STS will evaporate back to HNO_3 when temperature rises. NAT falling out of the stratosphere is the main sink term for total (gas + particle) HNO_3. In addition, the HNO_3 abundance is affected by mixing across the vortex edge during sudden stratospheric warming (SSW) [*Matsuno*, 1971] and the reformation of $ClONO_2$ in later season [*Brakebusch*, 2013].

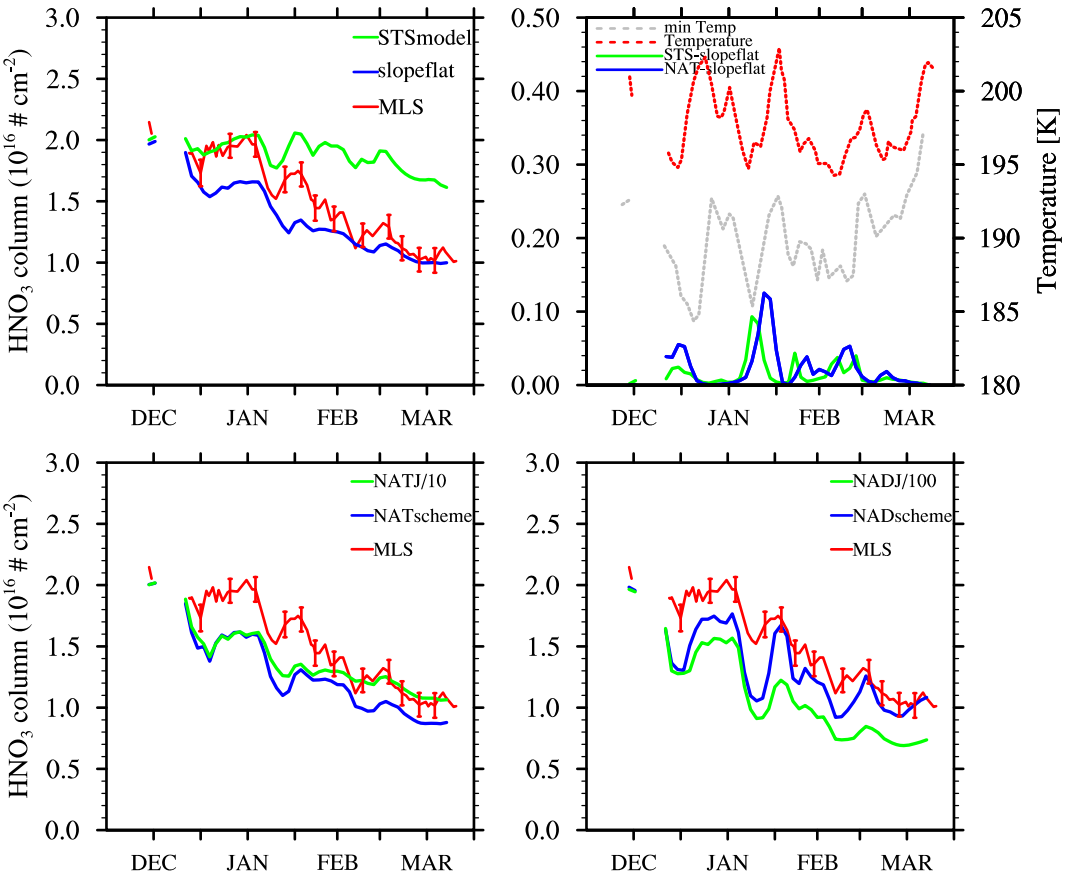

Figure 12. (top left and bottom) The gas phase HNO_3 concentration in the vortex column from MLS data (red), compared to simulations with different nucleation schemes. The MLS error bars show the vortex column systematic error. (top right) The condensed phase HNO_3 (expressed as the vortex column number of HNO_3 molecules with units, following the far left axis, of 10^{16} #/cm^2) in STS (green) and NAT (blue), respectively. Note that condensed phase nitric acid is less than 10% of the vapor phase. In the top right plot, the vortex average temperature at 475 K potential temperature [*Brakebusch*, 2013] is marked as red dots; the minimum temperature is given as grey dots.

As mentioned previously, we find that only a very small number of STS particles nucleate to form NAT and as a consequence the NAT surface area is much smaller than the STS surface area on average (they are often spatially separated, so NAT can dominate locally). As a result NAT is generally unable to reduce the gas phase partial pressure to the NAT vapor pressure unless it is present for a substantial period of time.

In contrast, if NAT particles nucleate quickly and convert a significant number of STS particles to NAT, then they very quickly will reduce gas phase HNO_3 below the STS vapor pressure and pull HNO_3 from the gas phase and from STS. In this case, reducing the nucleation rate will create fewer NAT particles with bigger radii, which likely increases the denitrification as illustrated in the top two plots of Figure 11. However, the slow nucleation scheme in our model, shown in bottom two plots of Figure 11, does not lead to a sudden dramatic reduction in partial pressure in the gas phase. In this case, decreasing the nucleation rate does not affect the size of the particles very much. Therefore, reducing the nucleation rate decreases the denitrification.

In order to compare the chemistry and PSCs occurring inside the polar vortex with data, we define the vortex using scaled potential vorticity (sPV) [*Dunkerton and Delisi*, 1986; *Manney et al.*, 1994] values greater than 1.4×10^{-4} or 1.7×10^{-4} s^{-1}. sPV is calculated by using the GEOS5 wind field for both model and MLS observations. The vortex average method for MLS data applies sPV of 1.4×10^{-4} s^{-1} [*Brakebusch*, 2013]. sPV's calculation for MIPAS observations uses the European Centre for Medium-Range Weather Forecasts (ECMWF) high-resolution ERA-interim meteorological products [*Arnone et al.*, 2012]. The vortex average method applies sPV of 1.7×10^{-4} s^{-1} for MIPAS data described by *Arnone et al.* [2012].

Figure 12 shows the HNO_3 partial column abundance from 400 to 700 K potential temperature averaged over the polar vortex based on gas-phase HNO_3 data from MLS and simulations with the SD-WACCM/CARMA model using several NAT nucleation schemes. It is possible that comparing the column amount of nitric acid in the model and observations might be misleading because of possible compensating errors in different parts of the column. Below we also discuss the vertical profile of the nitric acid to alleviate this problem.

The STS-only simulation of nitric acid in Figure 12 (top left, green) shows the situation in which no NAT forms. While the gas phase column declines when gas is converted to particles, there is no significant loss of nitric acid from sedimentation over the winter because the STS particles are small (which we have confirmed with a simulation with no fall velocity-not shown). Rather, the difference between the HNO_3 column between the start and end of winter for the STS-only case is due to dynamical transport between the vortex and its surroundings. Therefore, the difference between the STS case and the MLS observations (red) at the end of winter, when no PSCs remain, represents an estimate of the permanent denitrification caused by NAT particles. From December to late March, almost 50% of the nitric acid column is lost comparing the STS-only case and the MLS data inside the vortex from 400 to 700 K potential temperatures.

The simulations with different NAT nucleation schemes in Figure 12 show how important the nucleation scheme is to the denitrification. An interesting feature of the data is that very low average temperatures and low minimum temperatures at 475 K occur in late December with little denitrification. However, similarly low temperatures occur in January and February that do lead to denitrification. Comparing the denitrification simulated using the NATscheme, NADscheme, and reduced rates (NATJ/10 and NADJ/100), we find that NATscheme is a slow nucleation scheme (reducing the rate reduces denitrification) and NADscheme is a fast nucleation scheme (reducing the rate increases denitrification). Among the five cases tested, the slopeflat case and NATJ/10 are closer to MLS data than the others. But, the nitric acid in the gas phase in NATJ/10 increases in February and March, which indicates insufficient denitrification at that time. The HNO_3 line for the NADscheme decreases sharply when PSCs are present. As a fast nucleation scheme, the NADscheme nucleates many NAT particles, which take up HNO_3 rapidly from the environment (the NADscheme nucleates NAD particles, but we assume NAD transforms to NAT immediately). Those NAT particles contribute to the temporary denitrification but cannot grow very big due to their large number density. They evaporate back to gas phase when temperature goes up and the HNO_3 remains at similar pressure levels to the original one. This explains why the nucleation rate between the NATJ/10 and the NAD schemes differ by 4 orders of magnitude (Figure 3), while the denitrification at the end of the season is about the same.

There are several additional factors that can impact the denitrification rate, beyond the number of NAT particles. Using the slopeflat nucleation rate, we vary the temperature, the sticking coefficient, the NAT particle mass density, and the NAT particle shape (see Table 1) to see how these parameters affect the denitrification. Figure 13 shows the HNO_3 column for these three simulations compared with the base slopeflat simulation and MLS observations. The denitrification decreases when we reduce the sticking coefficient for NAT growth. The sticking coefficient reduces the growth rate of NAT, which yields lower-mass particles with reduced fall velocity. When we reduce the NAT particle density or change the shape to flat plates, the denitrification increases. Reducing the density increases the size of particles, which leads to a larger growth rate and more denitrification. The shape of the particle influences the fall velocity [*Pruppacher and Klett*, 1997]. Generally, the nonspherical shape decreases the fall velocity because of the increased drag force [*Cheng et al*., 1988]. When we change the NAT particle shape from spherical to a flat plate, the enhanced particle surface area not only decreases the fall velocity, but also the growth rate increases relative to a spherical particle. Hence, for reduced particle density and changed shape, the decrease in fall velocity at a fixed radius is overcome by the increase in radius due to increased growth rate.

The bottom right plot in Figure 13 shows simulations with reduced temperature as well as reduced temperature and sticking coefficient. When we apply a 1.5 K reduction to the heterogeneous chemistry as described by *Brakebusch* [2013] and CARMA microphysics processes, the denitrification increases strongly because the area of the vortex with STS particles increases resulting in a higher nucleation rate of NAT. The grey line shows a case with a 1.5 K temperature reduction and with a sticking coefficient for nitric acid on NAT of 0.2 [*Crowley et al*., 2010]. In this case, the nitric acid column is similar to that from the baseline

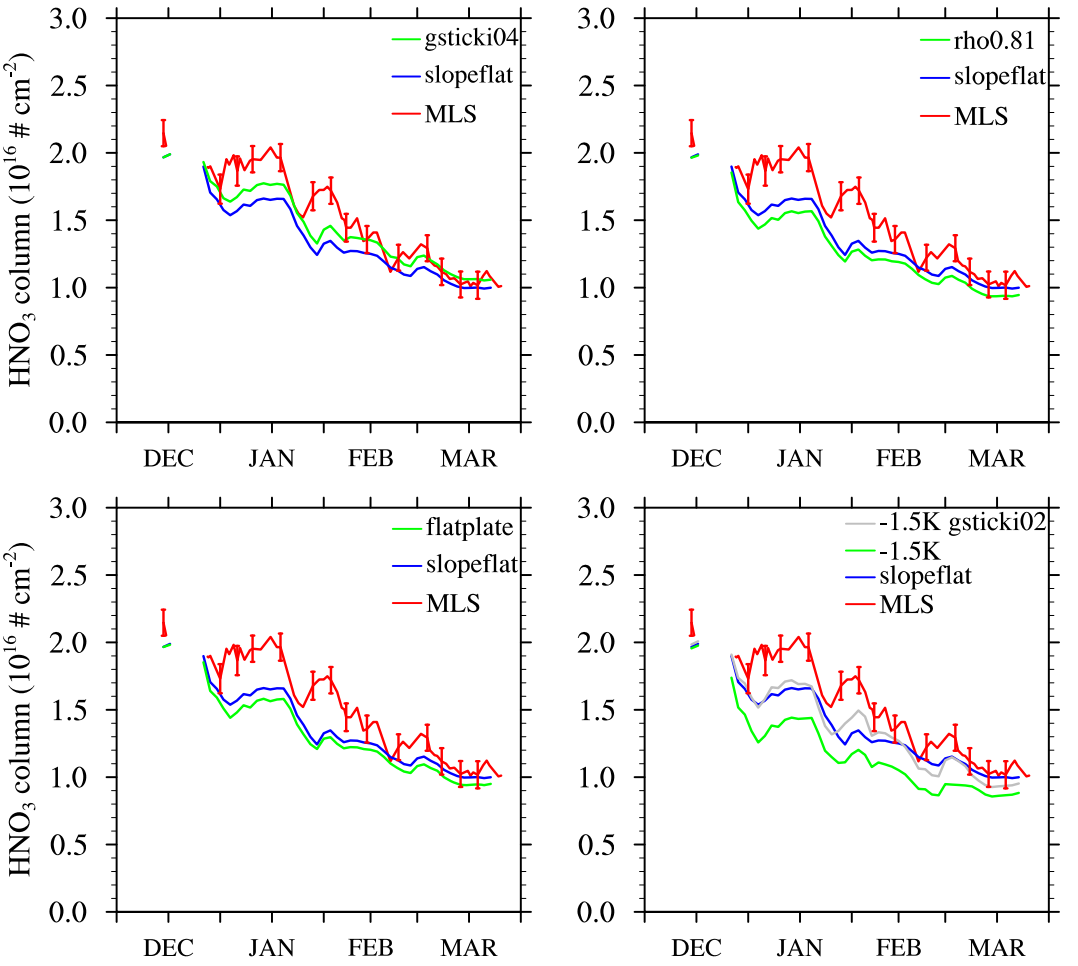

Figure 13. The gas phase HNO_3 column concentration inside the vortex from MLS (red), and simulations using the slopeflat nucleation and the cases that tune the parameters based on slopeflat case. The MLS error bars show the vortex column systematic error.

temperature. In summary, the denitrification is very sensitive to the temperature, which limits the ability to use observations to constrain microphysical parameters such as the nucleation rate and the sticking coefficient.

Further information linking the nucleation rate and particle properties can be gained by examining the HNO_3 seasonal variation as a function of altitude (potential temperature). Figure 14 shows the vortex average gas phase HNO_3 volume mixing ratio on different potential temperature surfaces from December to March from MLS data, MIPAS data [*Arnone et al*., 2012], and a simulation using the slopeflat nucleation rate.

The simulation compares well with MLS and MIPAS data on the 550 K level (about 22–23 km) though there is too much nitric acid in February and March. The model (Figure 2) shows a consistent warm bias at this level for February and March. Also, it denitrifies too much at lower altitudes (475 and 400 K), especially at 400 K. This difference in nitric acid may again be due to the cold temperature bias in the model at these levels (Figure 2). As a result of the cold bias, the NAT particles cannot evaporate fast enough to return the nitric acid back to the gas phase around 400 K. Instead, the NAT particles fall out of the stratosphere. However, the sensitivity tests by *Woiwode et al*. [2014] indicate that the renitrification at the lower altitude is not very sensitive to ± 1 K temperature bias. Instead, the falling velocity of NAT is important for simulating the renitrification of HNO_3. In our test cases, we tune the falling velocity by changing the particle density, the NAT shape and sticking coefficient influence the falling velocity. But in all cases, less denitrification at lower altitudes results in not enough denitrification at higher altitudes. Therefore, the falling velocity cannot resolve the missing renitrification in our model. Another possibility is that our model only simulates large NAT

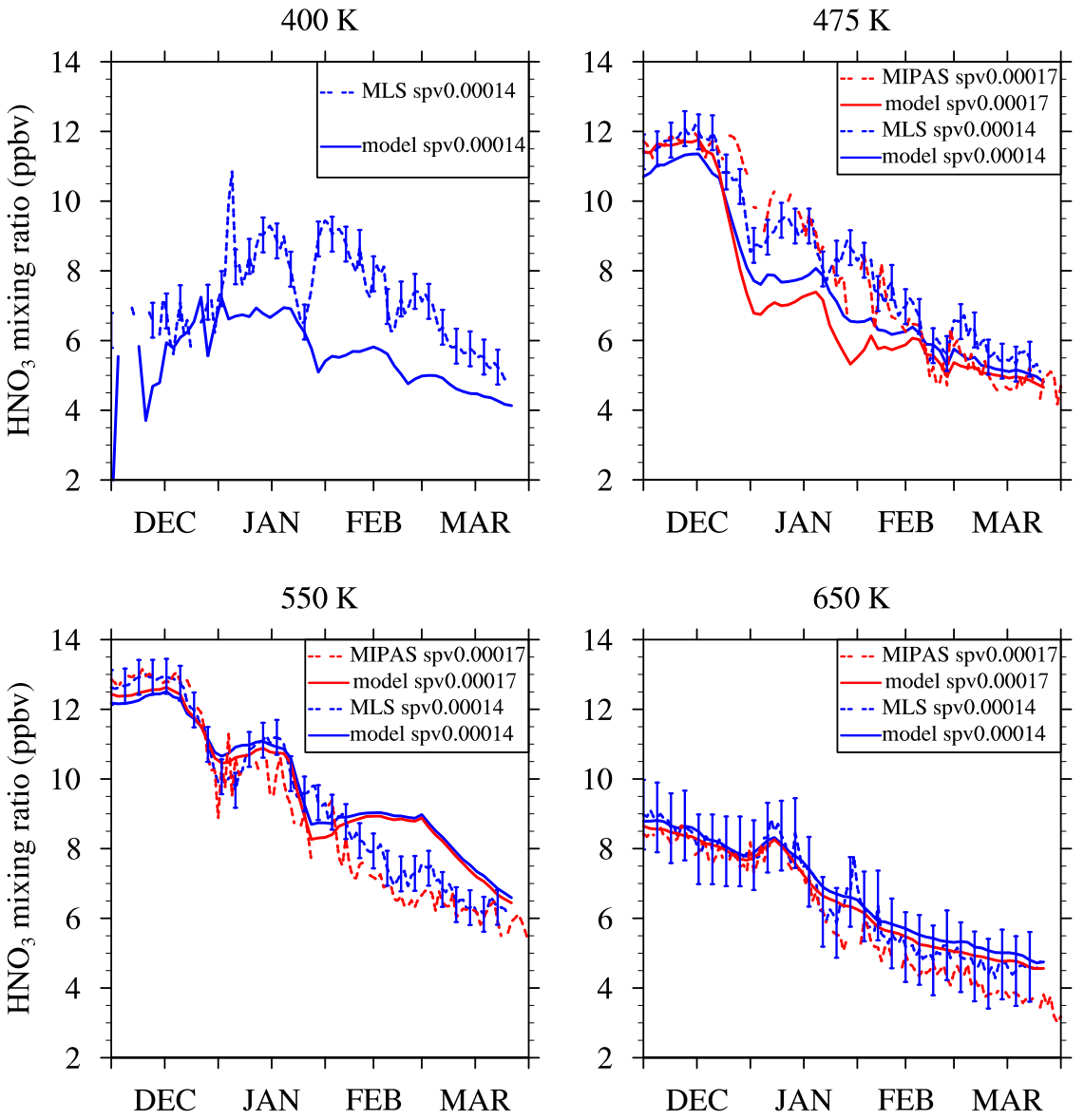

Figure 14. The vortex average HNO_3 gas mixing ratio from MLS, MIPAS [*Arnone et al.*, 2012], and a model case slopeflat at different potential temperatures. The MLS error bar shows the systematic error assuming one standard deviation of 0.5 ppbv for 400–550 K and 1 ppbv standard deviation for 650 K.

particles, while the real situations may contain both large and small NAT particles. The smaller sizes can evaporate faster and fall slower.

The overestimation of temporary denitrification in January and February at 475 K can be caused both by particles falling from levels above uptaking the HNO_3 and by the nucleation and growth of NAT at 475 K itself. Tests we conducted show that the denitrification at 475 K is mainly caused by the particles falling down to 475 K and their subsequent further growth at this level. We conducted a test (not shown) in which we did not allow nucleation of NAT at 475 K. The denitrification at this level improves less than 10%. When we reduce the sticking coefficient for NAT to 0.4 or we reduce the nucleation rate by a factor of 3 for levels above 475 K, the HNO_3 mixing ratio can match MLS and MIPAS well at 475 K. However, these tuning methods also influence the 550 K NAT nucleation and growth. Therefore, the underestimate of HNO_3 at 475 K at the end of December might suggest the need for a better nucleation equation or better parameters for growth, or a more accurate temperature history.

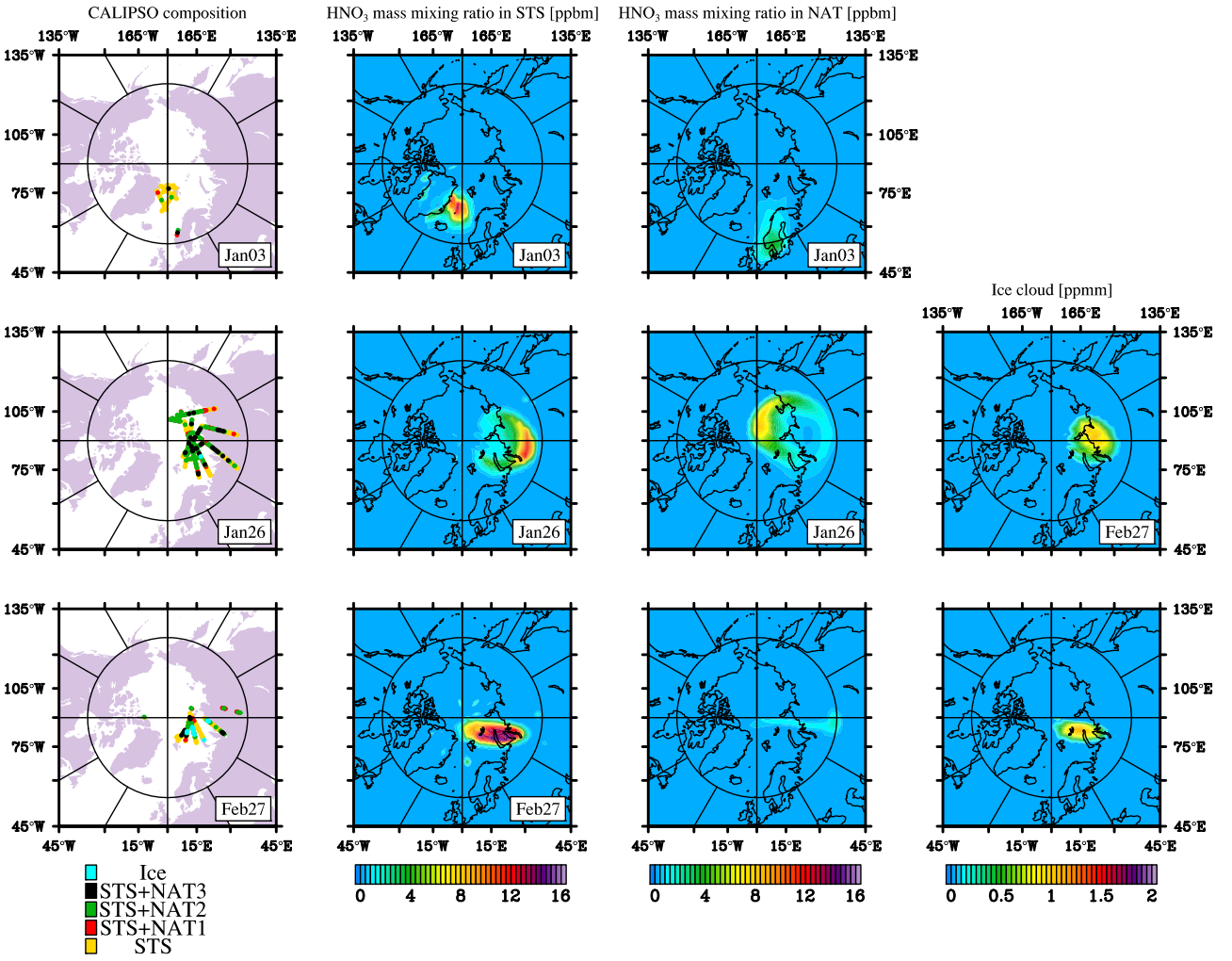

Figure 15. Polar view plots of (first row) CALIPSO-retrieved PSC composition, (second row) HNO_3 inside STS particles, (third row) HNO_3 inside NAT particles, and (fourth row) ice mass mixing ratio. The data for 3 January are at 22 km and model output at 26 hPa (∼22 km) at 00:00 GMT, 4 January 2011. For 26 January and 27 February, the data are at 20.5 km and the model output is at 36 mbar (∼20.5 km) at 00:00 GMT, 26 January 2011 and 27 February 2011. The CALIPSO composition marked as STS+NAT1 is STS with little NAT; STS+NAT2 is STS with intermediate NAT; STS+NAT3 is STS mixed with a large amount of NAT.

At 650 K, our model overestimates HNO_3 during the winter and finds that it increases in time (not shown in figures). Since PSCs rarely form at this altitude (near 26–28 km), the increasing HNO_3 is due to the heterogeneous chemistry occurring on the surface of sulfate aerosols. In this winter, the STS forms until 26–27 km only at the beginning of January (see Figure 19 and 21 below). In Figure 14 (and in all other simulations in this paper), we divided the sulfate aerosol surface area density (but not STS surface area density) by a factor of 4 for the heterogeneous chemistry at potential temperatures larger than 650 K. We choose a factor of 4 so that the surface area in our model is similar to that used in the standard WACCM model without CARMA. In that model, the surface area density of sulfuric acid aerosols is interpolated to the model grids based on the CCMVal2 recommendations [*Eyring et al.*, 2008]. However, the database has missing data at high-latitudes polar regions. These gaps are filled by a liner interpolation method [*Eyring et al.*, 2008]. With this change, the simulations agree well with the MLS and MIPAS data at 650 K. As we discussed in the section 1, cold sulfate aerosols are important for chlorine activation. Unfortunately, there are no data on the sulfate surface area at these altitudes, latitudes, and times. There are also limited data on the sulfur cycle in the upper stratosphere. These simulations indicate subtle problems with the sulfate cycle in the middle stratosphere in our model that are important to resolve in the future for simulations of the ozone budget.

Considering only homogeneous nucleation, most of the cases considered in Figure 12 predict large permanent denitrification in December and January, in contrast to the observations. The slopeflat case is the best

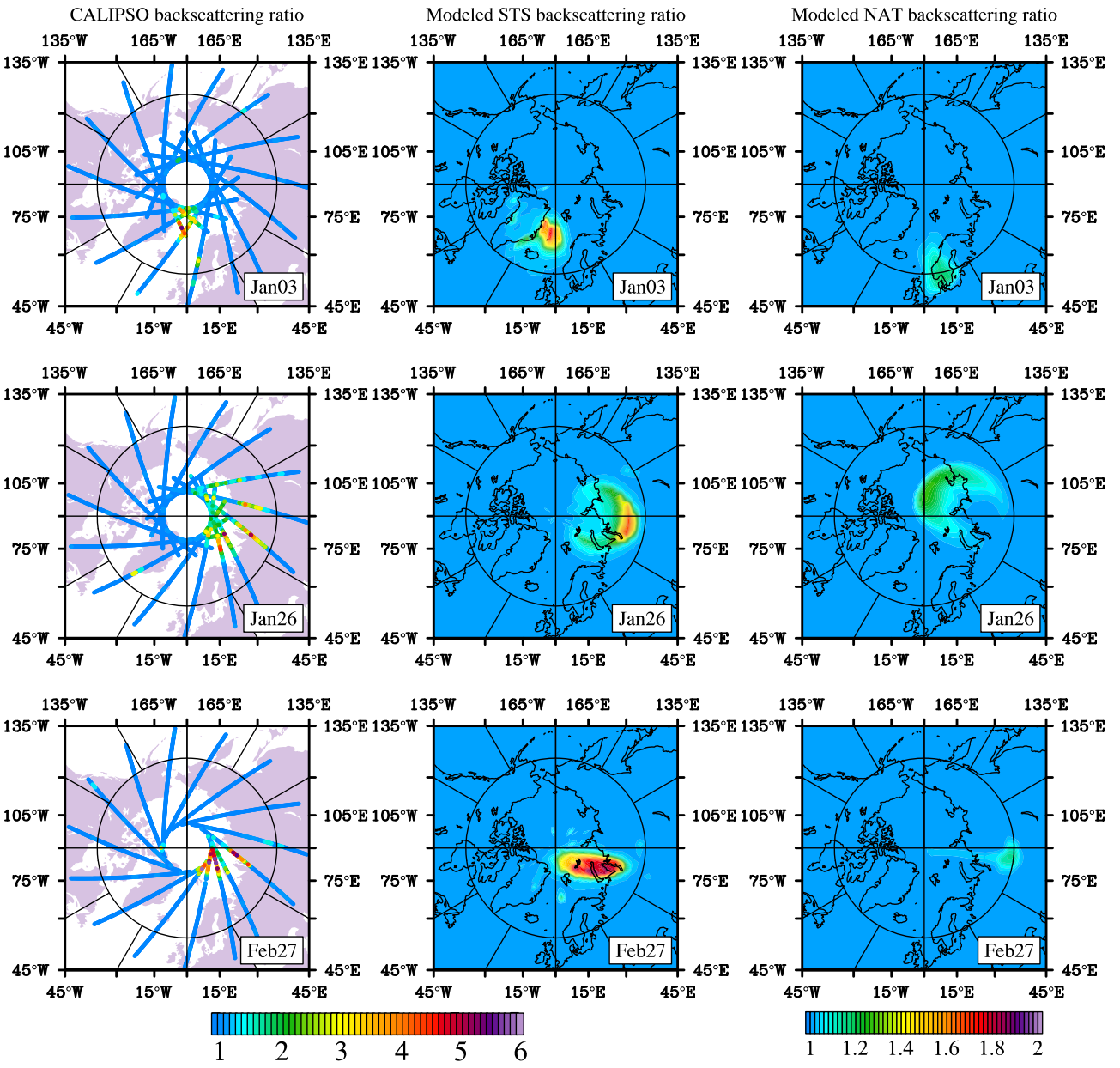

Figure 16. (left) The CALIPSO backscattering ratio, (middle) the modeled STS backscattering ratio, and (right) the modeled NAT backscattering ratio assuming spherical NAT particles. The altitude and the time is the same as in Figure 15.

in predicting the denitrification for the winter of 2010–2011, and the relative lack of denitrification in December.

Figures 15–18 compare PSC properties from the slopeflat simulation with CALIPSO data on 3 January at about 26 hPa (∼22 km), 26 January at 36 mbar (∼20.5 km) and 27 February at 36 mbar (∼20.5 km). Figure 15 shows the CALIPSO composition, the modeled HNO_3 mass in STS and NAT, along with the ice mass mixing ratio. The CALIPSO composition marked as STS+NAT1 is STS with little NAT; STS+NAT2 is STS with intermediate NAT; STS+NAT3 is STS mixed with a large amount of NAT [*Pitts et al.*, 2011]. On 3 January, an STS cloud was located just east of the coast of Greenland, where temperatures are lowest, while a NAT cloud was observed over Southern Norway and Sweden. The same cloud pairing can be found on 26 January and 27 February (Figure 15): the largest mixing ratios of HNO_3 in STS and NAT are often separated with a small

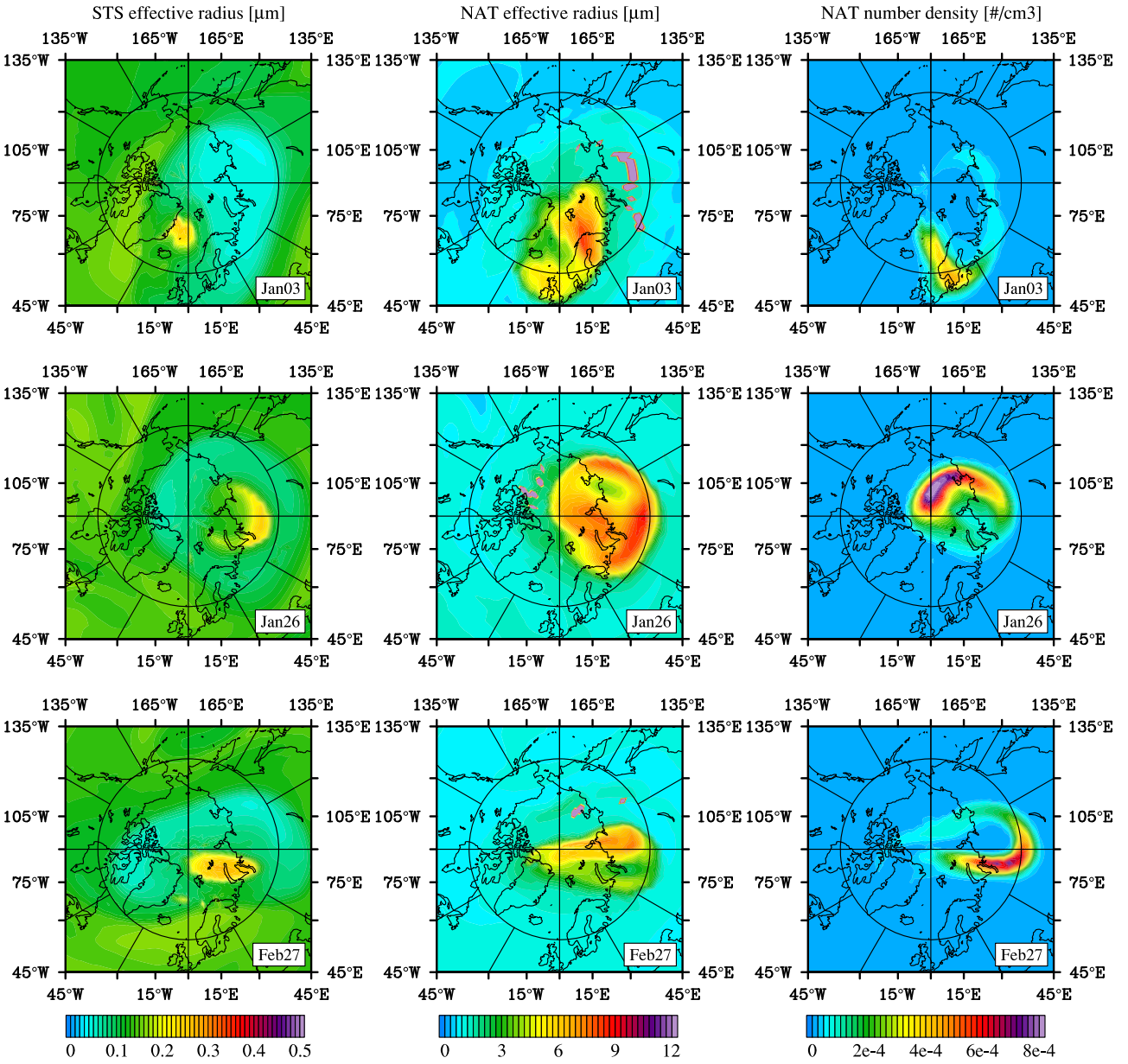

Figure 17. The modeled (left column) STS effective radius, (middle column) NAT effective radius, and (right column) NAT number density. The altitude and the time is the same as in Figure 15.

amount of mixed clouds in between. This is a consequence of the slow growth rate of NAT. NAT is nucleated in the location of the STS cloud in the previous days. NAT has a lower vapor pressure and, once formed, exists at higher temperature than STS. However, it takes considerable time for NAT to take nitric acid from the STS cloud. Therefore, for 3 January, for example, as the temperature increases along the streamlines from Greenland to Norway, the mass in the STS cloud slowly fades away, and the STS cloud is replaced by an equally massive, but optically inferior, NAT cloud. At the same time, new STS particles grow at locations with cold temperatures along the Greenland coast. However, CALIPSO often observes mixed clouds (red, green, and black dots in Figure 15) [*Pitts et al.*, 2009, 2011]. No ice particles are detected on 3 January at 26 mbar for both CALIPSO and the model. On 26 January, CALIPSO observes a little ice cloud near the Russian islands located at about 90°E, while the simulations produce a larger range of ice clouds. On 27 February, both CALIPSO and the simulation show about the same coverage of ice clouds near the Russian islands.

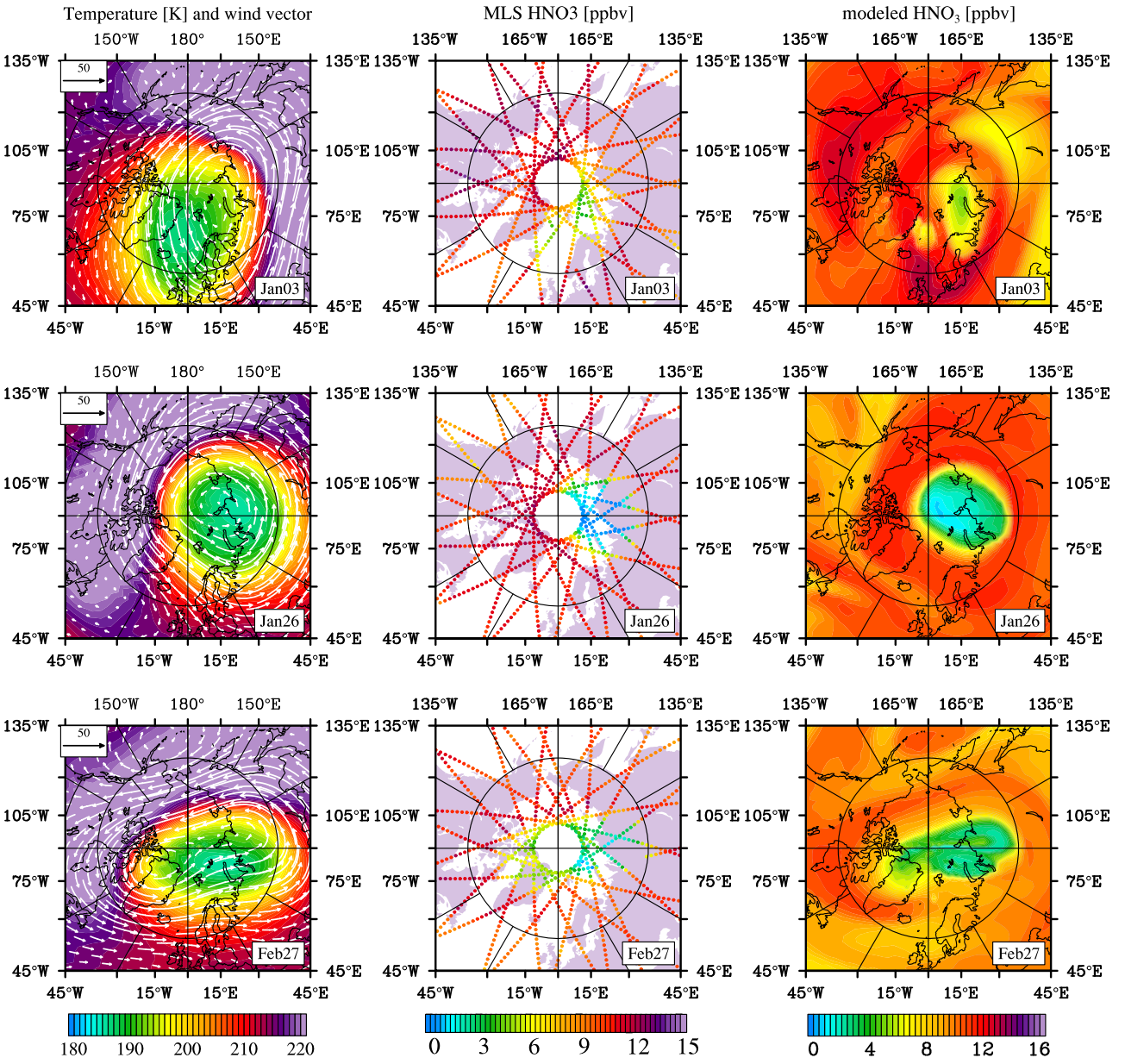

Figure 18. The modeled (left column) temperature and wind vector, (middle column) the MLS HNO_3 mixing ratio, and (right column) HNO_3 mixing ratio. The altitude and the time is the same as in Figure 15.

Figure 16 shows the STS backscattering ratio, the NAT backscattering ratio assuming spherical particles, and the CALIPSO backscattering ratio at the same time and location as Figure 15. It would be better to treat the NAT particles with nonspherical optical models. However, the shape of NAT particles, and its variation in time and space, is not known. We plan to explore this issue in future work. To calculate the backscattering ratio for modeled PSCs, we use the number density and particle radius from the model results and apply the Mie code by *Bohren and Huffman* [1983]. The estimated refractive indices for STS [*Luo et al.*, 1996] are [1.32, 1.35, 1.38, 1.40, 1.42, 1.435, 1.447, 1.45, 1.45, 1.45, 1.45] for STS from 0% to 100% HNO_3 weight percent in 10% increments for all temperatures. For simplicity, even though NAT is nonspherical, we assume it to be spherical (and therefore cannot derive a depolarization ratio) with a constant refractive index of 1.43. The backscattering ratio is the ratio of the aerosol plus molecular backscattering divided by the molecular backscatter. Figure 16 shows that the magnitude of the backscattering ratio of STS and NAT particles in the

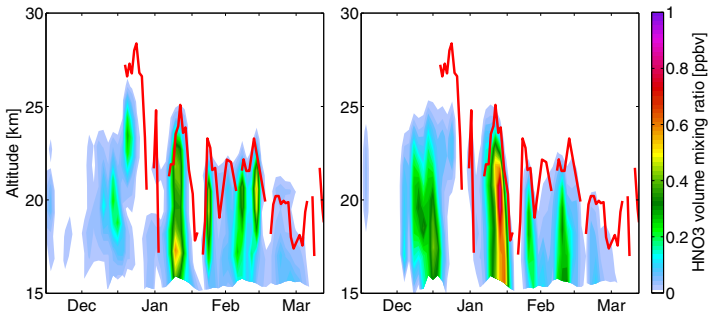

Figure 19. HNO_3 vortex average volume mixing ratios (contours) in (left) modeled STS and (right) modeled NAT are not compared with mixing ratio from SCIAMACHY but only PSC occurrence height (red lines) [*Hommel et al.*, 2014]. SCIAMACHY observations are retrieved for the PSC altitude from 1 January 2011 to March 2011, and are identical in the left and right plots. The absence of contours at 15–16 km is missing data rather than values near zero of HNO_3 mixing ratio due to poor definition of the polar vortex below this level.

simulation is consistent with the CALIPSO observations. Both the observations and the modeled STS backscattering ratios show a maximum value of ∼5.

Figure 17 presents the STS and NAT effective radius, and NAT number density for the same conditions as Figure 15. The effective radius of STS particles is about 0.2–0.3 μm and NAT effective radius is ∼5μm for the locations with maximum HNO_3 abundance and number density. Figure 18 presents the temperature and wind vectors, the MLS HNO_3, and modeled gas phase HNO_3 for the same conditions as Figure 15. The features of areas of reduced gas phase HNO_3 are well simulated compared with MLS observations on the days shown.

Figure 19 shows the vortex average volume mixing ratio of HNO_3 from the model compared with SCIAMACHY observations [*Hommel et al.*, 2014] at the altitude of PSCs. The highest altitudes of PSCs from the model are consistent with the observations. Also, the times of formation and disappearance of PSCs agrees with the observations, with the exception of the period after 15 March, when the model does not have PSCs. With SCIAMACHY, the highest altitude of PSCs declines from about 28 km in early January to near 20 km in mid-March. The model has a similar behavior, though PSCs only reach about 26 km in early January.

The surface area density (SAD) is important for the heterogeneous chemistry occurring on the surface of PSC particles. Figure 20 shows the modeled vortex average SAD of STS and the maximum SAD of STS. The average SAD has the peak at an altitude around 400 K over the season. The SAD magnitudes and locations mimic the patterns in the STS mass mixing ratio shown in Figure 15. The surface area of NAT particles (not shown) is nearly zero (about 2 orders of magnitude lower than SAD of STS particles).

Figure 21 shows the time dependence of the volume of air that is occupied by PSCs during the winter of 2010–2011. In this case, the model defines a PSC to be continuous over a grid cell at the mean value, and a PSC to be present if the backscattering ratio is greater than 1.32 or NAT is present with more than 5 ppbm HNO_3 inside the particles. This volume is compared with observations from CALIPSO which defines a PSC to

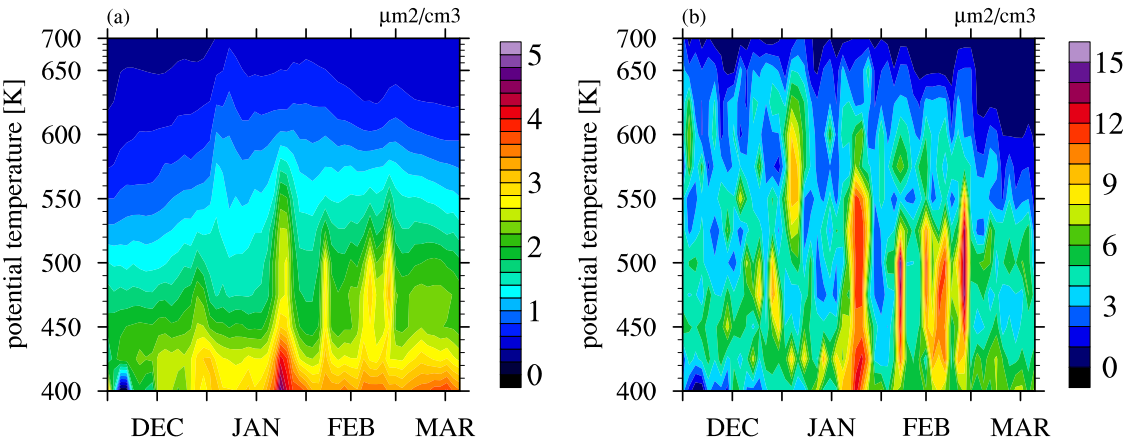

Figure 20. The simulated surface area density as a function of potential temperature and time. (a) The vortex average surface area for STS particles; (b) The maximum surface area for STS particles.

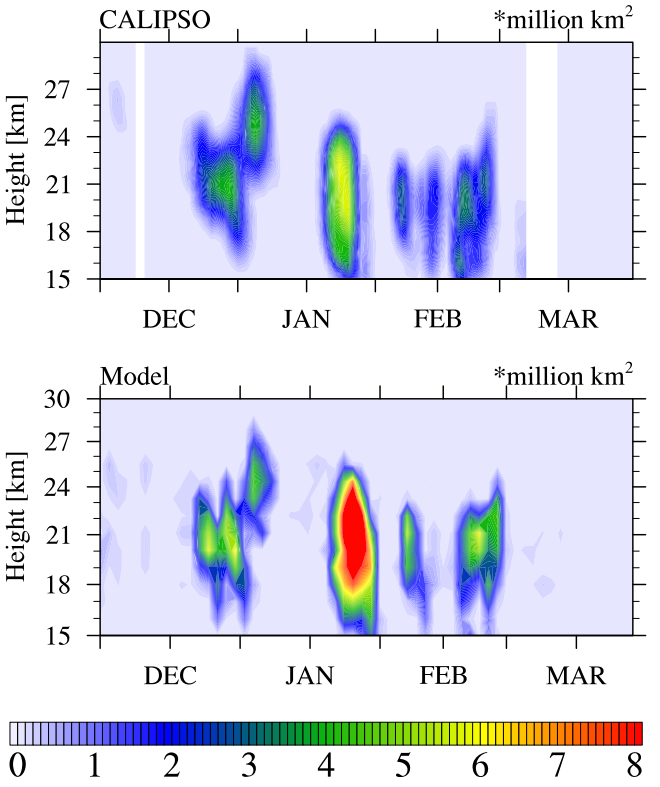

Figure 21. Evolution of PSC area coverage during the 2010–2011 Arctic winter from (top) CALIPSO and (bottom) the model. The blank parts in the CALIPSO plot represent missing data.

be present if the backscattering ratio is higher than 1.32 for horizontal smoothing scales of 135 km [*Pitts et al.*, 2009], which is close to the resolution of our model. CALIPSO uses both backscattering ratio and perpendicular backscatter for PSC identification. The detailed thresholds for different spatial resolution are described by *Pitts et al.*, [2009]. We exclude the areas north of 82°N from our model, because CALIPSO cannot observe those high latitudes. The model shows consistent cloud locations and cloud amounts compared with CALIPSO data. In early March, both the model and CALIPSO indicate spatially limited PSC cloud formation around 15 to 18 km, which forms due to the prolonged cold vortex for this winter. In late January, the model has cloud coverage of 8 million km^2 while CALIPSO detects about 6 million km^2. Also, the model misses a spatially limited PSC cloud formation event in mid-February. In Figure 19, NAT has large concentrations in these two periods. CALIPSO cannot detect some areas with large NAT particles at low number densities. The

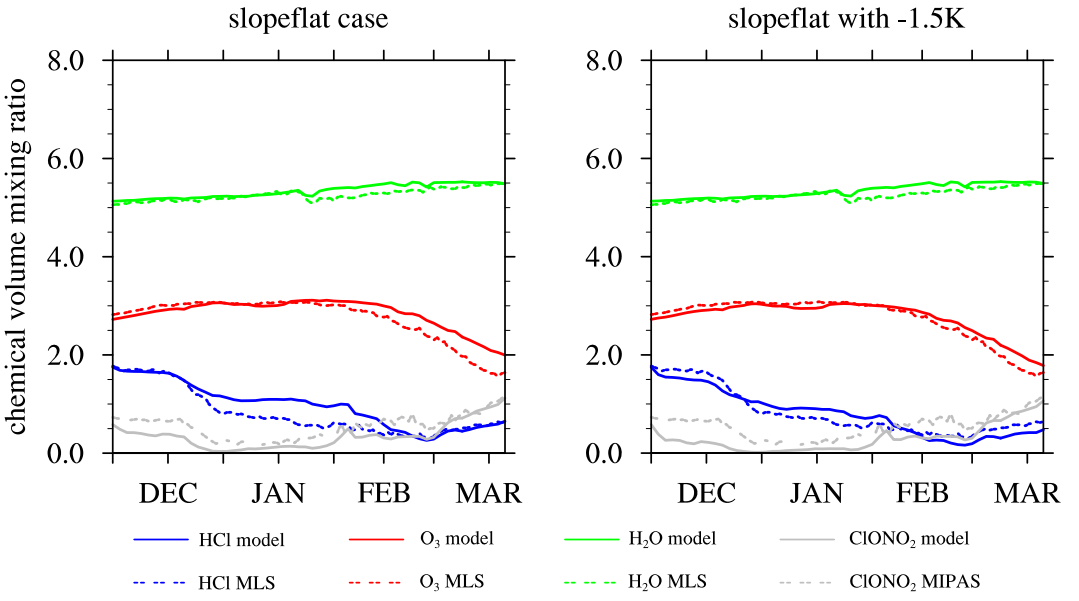

Figure 22. Evolution of vortex average mixing ratios of ozone-related chemicals at 475 K in base case and a case with −1.5 K adjustment in temperature for heterogeneous chemistry and PSC formation. H_2O and O_3 are in ppmv; HCl and $ClONO_2$ are in ppbv. The criteria for scaled potential vorticity for MLS data and its correspondent model results is 0.00014; and for MIPAS data [*Arnone et al.*, 2012] and its correspondent model results is 0.00017.

temperature bias in the model may be another possible reason resulting in NAT formation that is different from the observations in Figure 21.

4.3. Ozone-Related Chemicals

Ozone and its related chemicals are influenced by heterogeneous chemistry occurring on the surface of PSCs and of sulfate aerosols. These reactions depend both on reaction rates and on the surface area of the PSCs and sulfate aerosols.

The evolution of the chemicals involved in ozone loss is another indicator that PSCs are properly simulated. Figure 22 shows the O_3, HCl, H_2O, and $ClONO_2$ average volume mixing ratios inside the vortex from two slopeflat cases, which differ by the temperature assumed, compared with MLS and MIPAS data. We chose to examine the lower-temperature case because *Brakebusch et al.* [2013] found that important modeled reaction rates produced more realistic results with the lower temperature. Water vapor in our model is treated by the WACCM hydrological scheme. Water vapor mainly responds to the air temperature, but shows little difference between the two simulations. In the slopeflat case, the H_2O mixing ratio (green lines) from WACCM is within 5% of the MLS observations, which is within the uncertainty of the data. The HCl matches the observations at the beginning and the end of the season. However, the simulation is about 50% higher than the observations in January and February. One possible reason for this difference is that HCl is soluble in STS particles, which has not been considered in the growth process in our PSC model. A more likely reason is that the model does not have enough $ClONO_2$ at the beginning of the winter to react with HCl and deplete the HCl mixing ratio down to the observed levels [*Brakebusch*, 2013]. The model overestimates ozone at 475 K by about 25% at the end of the simulations, probably because of the temperature bias in the model.

Brakebusch et al. [2013] show that the −1.5 K bias can significantly influence the heterogeneous chemistry reaction rates, because the uptake reaction coefficients in liquid sulfuric acid aerosols and STS change rapidly at the STS formation temperatures [*Shi et al.*, 2001; *Lowe and MacKenzie*, 2008]. The lower-temperature case does show better performance on ozone and HCl, though it does more poorly on $ClONO_2$ as shown in Figure 22, right. As discussed previously, the −1.5 K case produces too much denitrification (Figure 13), but that could be compensated by, for instance, reducing the sticking coefficient of HNO_3 on NAT to 0.2 (Figure 13).

5. Conclusions

STS and NAT particle microphysics have been added to the WACCM/CARMA sulfate model as an initial step toward building a complete PSC model. The model does not currently contain interactions between nitric acid and ice clouds. We posed three questions in the paper:

1. Can our model properly simulate the particle volume, size distribution, lidar backscatter, PSC composition, and other data related to the fundamental properties of the clouds that are important for ozone loss?
2. Can our model properly simulate the denitrification during the Arctic winter 2010–2011?
3. Can our model properly simulate the evolution of ozone and the related chemicals controlling ozone over the 2010–2011 Arctic winter?

In order to address question 1, the microphysical characteristics of the simulated STS and NAT particles have been compared with available observations. The total volume of STS particles versus temperature, as well as the STS volume size distributions, closely resembles the observations (Figures 7 and 8). The simulations often produce NAT particles with a radius bigger than 10 μm (Figure 9). Such large particles have been observed. The weight percent of HNO_3 in STS particles compares well with Carslaw's equilibrium model indicating the STS particles respond to the environmental temperature very quickly relative to a WACCM time step of 30 min and generally remains close to equilibrium (Figure 5). However, evaporating clouds and other clouds with modest surface areas of a few $\mu m^2/cm^3$ are not able to maintain equilibrium (Figure 6).

The simulated height of PSCs is within a few kilometers of the height of PSCs observed by SCIAMACHY. The area of the vortex south of 82°N that contains PSCs is similar to CALIPSO-retrieved cloud coverage. The simulated cloud coverage shows an overestimate in late January relative to CALIPSO. The overestimation

may be caused by different NAT definitions between the model and CALIPSO. Also CALIPSO cannot detect NAT particles with small surface areas.

In order to address question 2, we explored several nucleation rate expressions for NAT particles, which were constrained by the observed denitrification history for winter 2010–2011. The challenge in duplicating this history is that little denitrification occurred in December, but significant denitrification occurred in January, despite both periods having similar low temperatures at the altitude of the 475 K potential temperature surface, which is a common PSC formation altitude for this winter. The nucleation rate equations we considered were based on the NAT and NAD surface nucleation equations [*Tabazadeh et al*., 2002]. We find the nucleation rate is mainly dependent on the HNO_3 weight percent inside the STS particle rather than the temperature (note that HNO_3 weight percent is temperature dependent). The five nucleation rate expressions we considered have free energies within 10% of each other, but the nucleation rates vary by several orders of magnitude. The slopeflat case was the best scheme among those considered because the HNO_3 evolution in those simulations is the closest to MLS observations. We found that the denitrification is very sensitive to temperature variations at the 1.5 K level (Figure 13), which is within the errors of observed temperatures. When we apply a −1.5 K temperature bias in our model for heterogeneous chemistry and CARMA microphysics, the denitrification at all levels increases significantly because the temperature influences both the area of the vortex with STS particles and the NAT nucleation rate. Low temperatures could be somewhat compensated for using an uptake coefficient of 0.2, which slows the growth of the particles once they have nucleated and reduces the denitrification. Changing the shape of NAT particles to flat plates or lowering density, which should reduce the fall velocity, does not slow down the denitrification as might be expected because the increased particle area leads to larger growth, larger particles, and faster sedimentation.

The slopeflat scheme is a slow nucleation scheme, which means the particles initially nucleated do not have enough surface area to quickly pull nitric acid away from STS. As a consequence, the individual NAT particles do not compete with each other for vapor and grow to roughly the same size independent of the nucleation rate. As a consequence, the denitrification goes up when the nucleation rate increases. Another consequence of the low area is that considerable time is needed to transfer HNO_3 to the NAT. This slow growth, and even slower evaporation, of NAT results in STS clouds, with freshly nucleated NAT, being separated by large geographic distances from NAT clouds with similar mass mixing ratios as the original STS clouds. We find evidence that such NAT and STS clouds have independent locations in both simulations and in CALIPSO data (Figures 15 and 16). CALIPSO does indicate more STS and NAT mixed clouds than the model does, but this is difficult to quantify because of lack of information about how to represent the backscatter by nonspherical NAT particles. While the masses of the STS and NAT clouds are similar, the NAT clouds have 10–100 times less surface areas making them less chemically reactive, and more difficult to detect optically, than STS clouds.

Our model simulates stratospheric sulfates as well as PSC particles. We find that at altitudes corresponding to 650 K potential temperature that few PSCs form, and the sulfate surface area is large enough to impact heterogeneous chemistry for nitric acid and push the values well above those observed. While there are no data on the sulfate surface areas, we believe our model is not realistic because the high SAD in our model around 650 K results in an excessive production of HNO_3 through the heterogeneous chemistry compared with MLS and MIPAS observations. These results suggest both the potential importance of sulfate particles, and the need for models to do a better job simulating the stratospheric sulfur cycle.

The polar view of temporary and permanent denitrification in the slopeflat case is similar to MLS observations during three typical PSC formation days: 3 January at 26 mbar, 26 January at 36 mbar, and 27 February at 36 mbar (Figure 18).

We considered the third question by simulations of ozone in the year 2010–2011. Our model underestimates the ozone depletion in March compared with MLS observation, which is probably due to a high temperature bias in the model. A sensitivity test with −1.5 K adjustment [*Brakebusch*, 2013] improves the modeled O_3, which indicates a small temperature bias can significantly influence the heterogeneous chemistry reaction rates. The model also overestimates the HCl amount during January and February, which is probably because the model does not have enough $ClONO_2$ to react with HCl during these times. However, HCl is also better predicted with the 1.5 K temperature decrease.

There are a number of factors in our model that require improvement. The NAT nucleation is very sensitive to temperature, which makes it difficult to constrain microphysical parameters such as the nucleation rate and the sticking coefficient. The nucleation rate is so slow at relevant stratospheric temperatures that laboratory experiments to retrieve the nucleation rate are very difficult. Fewer than 1 in 1000 STS particles nucleate to form NAT. Our current model does not produce submicron NAT particles. We are currently ignoring mountain wave clouds as well as gravity waves. Gravity waves will produce thermal oscillations, which may trigger some NAT formation in STS clouds [*Tsias et al*., 1997]. Mountain waves are very important over the Scandinavian Peninsula [*Alexander et al*., 2013]. We believe our model picks up the longest wavelength waves, which respond to the entire mountain range, but there are many smaller, higher-amplitude temperature changes. These likely lead to the formation of some smaller NAT particles. We also do not include the interaction of nitric acid with water ice clouds. Submicron-sized NAT particles with large number density may be released as the ice evaporates [*Höpfner et al*., 2006]. Heterogeneous nuclei [*Hoyle et al*., 2013; *Grooß et al*., 2014] might be required for NAT nucleation, and stratospheric sulfates commonly contain micrometeorites. However, fully evaluating the possible impact of heterogeneous nuclei requires tracking the evolution of the nuclei, which has not yet been done.

Appendix A: Growth and Evaporation Process for STS and NAT Particles

The growth and evaporation rate equation [*Toon et al*., 1989] we use is similar to the expression by *Barkstrom* [1978] and *Ramaswamy and Detwiler* [1986]. In this equation, we ignore the effects of solutes on the vapor pressure and we ignore radiative heating of the particles:

$$\frac{dm}{dt} = g_0(p_\infty - A_k p_v)/(1 + g_0 g_1 p_v) \tag{A1}$$

Here $\frac{dm}{dt}$ is the mass growth rate (g/cm^3/s) for one particle, p is the partial pressure of the condensing gas infinitely far from the particle (e.g., environmental gas pressure), and p_v is the saturation vapor pressure (e.g., the pressure over a flat surface of the liquid in equilibrium with the gas). A_k is the Kelvin correction term, which represents the curvature effects of particles on the vapor pressure:

$$A_k = \exp(2M_c\sigma/RT\rho_s r)$$

Here σ is the surface tension, ρ_s is the particle density, M_c is the molecular weight of the appropriate vapor (water, nitric acid, or sulfuric acid), r is drop radius, the R is the gas constant, and T is the environment temperature.

The g_0 and g_1 terms in equation (A1) are growth kernels which include vapor diffusivity for the appropriate vapor (D), and thermal conductivity (K) considering the size of the particle relative to the mean free path, as well as the latent heat of condensation (L) [*Toon et al*., 1989]:

$$g_0 = 4\pi r D f_v M_c/(RT)$$
$$g_1 = M_c L^2/(RT^2 f_t K 4\pi r)$$

where f_v and f_t terms are ventilation factors to represent the effects of the motion of particles through the air on condensation and thermal conduction.

We use the full equations in our model for all particle sizes. For large particles, such as NAT, the equations have the dependencies that are obvious from the equations presented above. However, for sulfate and STS particles in stratosphere, the particle size (r) is generally smaller than the mean free path (H). At a typical stratospheric pressure of 50 hPa and temperature of 200 K, the mean free path is about 0.8 μm. That means the Knudsen numbers ($K_{nd} = H_d/r$ and $K_{nt} = H_t/r$) are often larger than 1 in stratosphere. In that case, the equations have different dependencies. The vapor diffusivity (D) and thermal conductivity (K) can be written as:

$$D = D' C/(r + \lambda C K_{nd}/\Phi_0)$$
$$K = K' C/(r + \lambda_t C K_{nt}/\Phi_0)$$

where

$$\lambda=(1.33+0.71/K_{nd})/(1+1/K_{nd})+1.33(1-\alpha_\alpha)/\alpha_\alpha$$
$$\lambda_t=(1.33+0.71/K_{nt})/(1+1/K_{nt})+1.33(1-\alpha_\tau)/\alpha_\tau$$

Here α_α (the sticking coefficient) and α_τ (the thermal accommodation coefficient) are assumed to be unity for STS [*Toon et al*., 1989]. Some data suggest that they may be less than one for HNO_3 condensing [*Crowley et al*., 2010]. *D′* is the temperature-dependent diffusivity of the appropriate vapor in air. The diffusion coefficient *D′* for water vapor is given by *Pruppacher and Klett* [1997]. For HNO_3, we use the similar expression [*Larsen*, 2000]:

$$D'_{HNO3}=A\times D'_{H2O}$$

In Larsen's paper [*Larsen*, 2000], *A* is 0.559. Here we tune *A* to match measurements for the diffusivity of HNO_3 in air at 296 K, 1 atm [*Tang et al*., 2014]. Here *A* is 0.466.

K′ is the thermal conductivity of air; and *C* is the capacitance of the particles [*Pruppacher and Klett*, 1997]. The definitions of Knudsen numbers can also be written as:

$$K_{nd}=H_d/r=3D'/(v_w r)$$
$$K_{nt}=H_t/r=3K'/(\rho v_t(C_p-0.5R)r)$$

Here, v_w is the mean thermal velocity of a water molecule and C_p is the heat capacity of air. Since we assume spherical particles, *C* has a value of unity, as does Φ_0, which is a shape correction for thermal diffusion. Therefore, for the stratospheric small particle limit, the diffusivity and conductivity can be simplified as:

$$D=D'/(\lambda K_{nd})=D'/(3\lambda D'/v_w r)=v_w r/(3\lambda)$$
$$K=K'/(\lambda_t K_{nt})=K'/(3\lambda_t K'/(\rho v_t(C_p-0.5R)r))=\rho v_t(C_p-0.5R)r/(3\lambda_t)$$

In the growth rate equation, we ignore the possibility that the vapor pressures might be modified by dissolved species such as HCl [*Toon et al*., 1986; *Weisser et al*., 2006] and micrometeorites, which could alter the vapor pressure for pure substances. When multiple species grow, we sum their growth rates. Strictly speaking the terms should not be summed because the latent heat release from the condensational growth of each species affects all the others. However, latent heat release is negligible for PSCs.

From equation (A1), we can get the particle growth/evaporation rate, and how much H_2SO_4 and HNO_3 mass should be moved between bins. Therefore, the aerosol continuity equation can be solved to obtain the new particle concentration:

$$\frac{\partial C(m)}{\partial t}=-\frac{\partial C(m)g(m)}{\partial m}$$

where *C(m)* is the concentration of particles with mass m; *g(m)* is the growth or evaporation rate for particles with mass *m*. Here *g(m)* is the same as $\frac{dm}{dt}$ in equation (A1). The meaning of the equation is that the rate of change of the particle concentration is determined by the divergence of the flux of particles moving from other masses to mass m and from mass m to other masses. A mass conserving, ratio conserving advection scheme [*Lin and Rood*, 1996, 1997] is used to solve this advection equation.

The growth equation requires equations for acid concentrations, vapor pressures and surface tensions among others to calculate the growth rate. These are described below.

A1. Acid Concentration

The acid concentration, or weight percent, is required to calculate vapor pressure, surface tension and solution density for ternary particles. The weight percent of HNO_3, H_2SO_4, and H_2O are based on Luo et al.'s scheme [*Luo et al*., 1995], which assumes that water vapor is in equilibrium with the particles.

There are several other models that consider either STS or binary sulfuric acid water vapor pressures and weight percentages. The Tabazadeh's scheme [*Tabazadeh et al*., 1997] has been successfully used to calculate the weight percent of sulfuric acid and aerosol size in the WACCM/CARMA sulfate model [*English et al*., 2011]. However, Tabazadeh's scheme does not consider a ternary solution. We find two schemes that treat

STS. We find that both *Luo et al.*'s [1995] and *Zhang et al.*'s [1993] methods agree well with Tabazadeh et al.'s scheme between 185 and 235 K assuming the HNO_3 amount is zero. However, the scheme of Zhang et al. is quantized and more time consuming to use in the model. Therefore, Luo's scheme is used in this STS-PSC model.

It is more complex to determine the weight percent when HNO_3 is present in the particles, and a vapor pressure equation is needed. We discuss this case in the next section.

A2. Vapor Pressures

We use the H_2SO_4 vapor pressure equation given by *Kulmala and Laaksonen* [1990], which is valid for a wide range of temperatures for a given weight percent solution. This formulation does not consider HNO_3 condensed on the particles. However, the vapor pressure of H_2SO_4 is very low for polar night temperatures, so it is not a limiting factor in condensational growth, although ignoring the effects of HNO_3 on the sulfuric acid vapor pressure might impact the sulfuric acid nucleation calculations.

The HNO_3 vapor pressure (in hPa) for STS particles is expressed as [*Luo et al.*, 1995]:

$$\ln p_{HNO3} = A_{HNO3} + B_{HNO3}/T + \ln[\omega_1(\omega_1 + 0.09\omega_2)]$$

where ω_1 and ω_2 are the weight percent of H_2SO_4 and HNO_3. A_{HNO3} and B_{HNO3} are constants and T is the temperature. CARMA tracks the abundance of H_2SO_4 and HNO_3 in each particle size class so the ratio of ω_1 and ω_2 is determined for each particle size class by CARMA.

We assume H_2O is in equilibrium with the particles so that the vapor pressure of water over the particles is also known. Given the water vapor pressure, and the ratio of ω_1 to ω_2, the empirical equation below contains only one unknown parameter, so it can be solved iteratively to determine the weight percent:

$$\begin{aligned}\ln p_{H2O} = {} & 23.306 - 4.5261\omega_1 - 5.3465\omega_2 + \omega_h(7.451\omega_1 + 12\omega_2) \\ & - \omega_h^2(4\omega_1 + 8.19\omega_2) + [-5814 + 1033\omega_1 + 928.9\omega_2 \\ & - \omega_h(2309\omega_1 + 1876.7\omega_2)]/T\end{aligned}$$

where $\omega_h = \omega_1 + 1.4408\omega_2$ and $\omega_1 = \omega_2 \times$ ratio.

The HNO_3 vapor pressure (in torr) for NAT particles is expressed as [*Hanson and Mauersberger*, 1988]:

$$Log_{10}(P_{HNO3}) = m(T) \cdot Log_{10}(P_{H2O}) + b(T)$$

where

$$m(T) = -2.7836 - 0.00088T$$

$$b(T) = 38.9855 - 11398/\mathrm{T} + 0.009179T$$

In the equations, temperature, T, needs to be in the range from 180 to 200 K. P_{HNO3} and P_{H2O} are in torr.

A3. Surface Tension and Density

The surface tension, γ, and the density, ρ, of ternary solutions are calculated by using empirical polynomial equations [*Martin et al.*, 2000]:

$$\gamma(x,y) = \left(\sum_{i=0}^{5}\sum_{j=0}^{5}\gamma_{i,j}x^i y^j\right)/(\gamma_0 + \gamma_1 x + \gamma_2 y)^2$$

$$\rho(x,y) = \sum_{i=0}^{4}\sum_{j=0}^{3}\rho_{i,j}x^i y^j$$

where $\gamma_{i,j}$, γ_0, γ_1, and γ_2 are the coefficients in the polynomial equation at temperatures of 293 and 253 K. x and y are the weight percent of H_2SO_4 and HNO_3 in each particle, respectively. Using the coefficients listed in *Martin et al.* [2000], we can calculate the surface tension and particle density of the ternary solution at 293 and 253 K for each bin. We assume the surface tension and the density depend linearly on temperature, and interpolate the surface tension and the density to other temperatures.

Appendix B: Coagulation Equation and Coagulation Kernel Setup in the Model

The basic coagulation equation is:

$$\frac{\partial C(m)}{dt} = \frac{1}{2}\int_0^m K_c(u, m-u)c(u)c(m-u)du - C(m)\int_0^\alpha K_c(u,m)C(u)du$$

The two terms on the right represent the coagulation production rate for particles of mass m due to coagulation of smaller particles and the second term is the loss rate of mass m particles due to coagulating to form larger particles.

K_c is the coagulation kernel. We use the Brownian coagulation kernel. A correction for the effect of Van der Waals forces between particles on Brownian coagulation [*Chan and Mozurkewich*, 2001] has been included in the CARMA model [*English et al*., 2011].

Although we use a general formulation, under the limit when the mean free path is much larger than the particle size (which roughly applies to sulfuric acid and STS particles), the Brownian coagulation kernel K_c is:

$$K_c = \alpha_s \pi (r_1 + r_2)^2 \sqrt{(v_1^2 + v_2^2)}$$

In this equation, two particles with radius r_1 and r_2 coagulate with each other with kinetic speeds of v_1 and v_2. α_s is the probability that the two particles will stick together. The coagulation kernel expresses the volume swept out by coagulating particles in a second and has units of $cm^3\ s^{-1}$. Figure B1 shows the coagulation kernel as a function of particle sizes at 50 hPa in the CARMA model. The coagulation kernel varies only slightly with pressure. The Brownian coagulation kernel ranges from 10^{-10} to 10^{-2} cm^3/s.

Appendix C: Sedimentation of Particles

The WACCM model transports the particles via resolved winds and eddy diffusion. However, the PSC vertical movement due to gravitational sedmentation and Brownian diffusion is simulated in CARMA:

$$\frac{\partial C}{\partial t} = -\frac{\partial (V_{fall} C)}{\partial z} + \frac{\partial}{\partial z}\left[\rho K_z \frac{\partial (C/\rho)}{\partial z}\right] \quad \text{(C1)}$$

where C is a given particle concentration in a fixed mass bin, V_{fall} is the fall velocity calculated in CARMA, and K_z is the Brownian diffusion coefficient. For Reynolds numbers less than 10^{-2} (particle radius less than about 10 μm, which is suitable for stratosphere sulfate aerosols and PSCs), CARMA uses the Stokes-Cunningham equation [*Toon et al*., 1989]:

$$V_{fall} = 2Br^2 \rho_p g/(9\mu)$$

where r is the radius of the particle, ρ_p is the density, and μ is the dynamic viscosity of air. B is the slip correction for the kinetic limit in which particles are smaller than the mean free path of air. For sphere, B is written as:

$$B = 1 + 1.246K_n + 0.42K_n e^{-0.87/K_n}$$

K_n is the Knudsen number, which is the ratio of mean free path and the particle radius. In the stratosphere, the sulfate

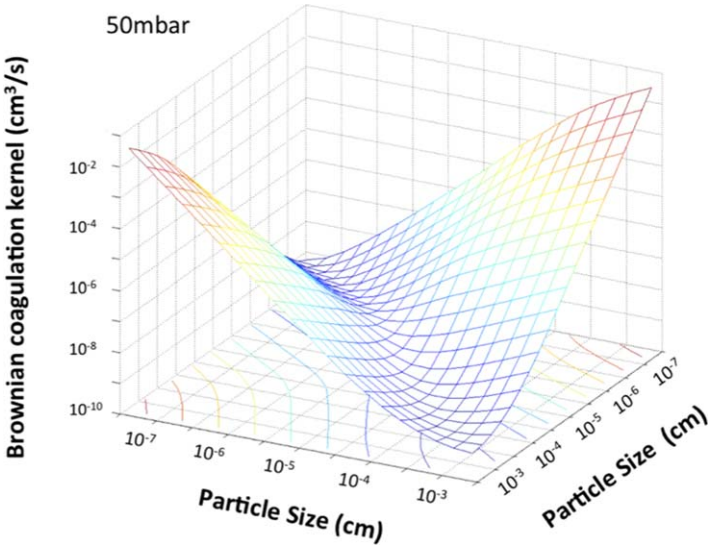

Figure B1. Brownian coagulation kernel at 50 hPa for particle sizes typical of polar sulfate aerosols and STS.

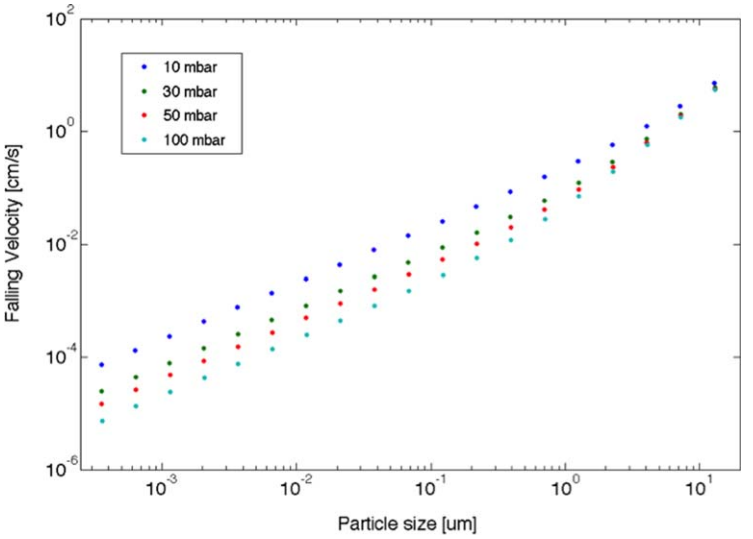

Figure C1. Fall velocity as a function of particle size at different stratospheric pressure levels.

particles are generally smaller than the mean free path (at a typical stratosphere condition with 50 hPa and 200 K, the mean free path is about 0.8 μm). For those particles which have large K_n, B is simplified as $B = 1.666K_n$ and the fall velocity equation can be written in kinetic limit:

$$V_{fall-kinetic} = \beta \rho_p g r / 2n_a \sqrt{\pi/(2m_a kT)}$$

where, n_a is the number density of air molecules; m_a is the mass of an air molecule; $\beta = 1.35$ for diffuse molecular scattering; $= 1$ for specular reflection.

For those particles which have large Reynolds number, the fall velocity equation needs to use the drag coefficient for correction. The relation between Reynolds number and drag coefficient is expressed by *Le Clair et al*. [1970].

The second term on the right of equation (C(1)) includes the Brownian diffusion coefficient. CARMA treats Brownian diffusion of aerosols, which is important above 100 km, and not well treated by algorithms in WACCM [*English et al*., 2011]. The vertical advection equation is solved by using the finite volume scheme to guarantee mass conservation and tracer ratio conservation [*Lin and Rood*, 1996, 1997].

Figure C1 shows the fall velocity as a function of particle size at different pressure levels, assuming the enviromental temperature is 200 K and particle density is 1.9 g/cm^3. The figure indicates that the STS particles, with a typical radius of 0.5 μm, have a fall velocity of $10^{-2}-10^{-1}$ cm/s, or about 0.3–3 km/month. While, NAT particles, with a size of 10 μm fall about 3 cm/s, or about 3 km/d. The high fall velocity of large NAT particles causes NAT particles to be important for denitrification.

Acknowledgments
MIPAS data are from the MIPAS2D database (www.isac.cnr.it/~rss/mipas2d.htm). We thank E. Arnone for his help with the MIPAS data. Data are provided courtesy of the National Centre for Earth Observation via the NERC Earth Observation Data Centre (NEODC). The work at the University of Colorado was supported by NASA grant NNX09AK71G, as well as a grant from the AURA satellite project. Work at the Jet Propulsion Laboratory, California Institute of Technology, was carried out under a contract with the National Aeronautics and Space Administration. We thank Lynn Harvey for her help with the MLS data. We thank Michael Pitts for his help with the CALIPSO PSC cloud coverage retrieval. We thank Stephan Borrmann and his group for their help with the PSC size data from the RECONCILE campaign. This work utilized the Yellowstone and Janus supercomputer. We would like to acknowledge high-performance computing support from Yellowstone (ark:/85065/d7wd3xhc) provided by NCAR's Computational and Information Systems Laboratory, sponsored by the National Science Foundation. Janus is supported by the National Science Foundation (award CNS-0821794) and the University of Colorado Boulder. The Janus supercomputer is a joint effort of the University of Colorado Boulder, the University of Colorado Denver and the National Center for Atmospheric Research.

References

Adriani, A., F. Cairo, M. Viterbini, S. Mandolini, L. Pulvirenti, and G. Di Donfrancesco (1999), Multiwavelength aerosol scatterometer for airborne experiments to study the optical properties of stratospheric aerosol, *J. Atmos. Oceanic Technol.*, *16*(10), 1329–1336, doi:10.1175/1520-0426(1999)016<1329:MASFAE>2.0.CO;2.

Alexander, S. P., A. R. Klekociuk, A. J. McDonald, and M. C. Pitts (2013), Quantifying the role of orographic gravity waves on polar stratospheric cloud occurrence in the Antarctic and the Arctic, *J. Geophys. Res. Atmos.*, *118*, 11,411–11,507, doi:10.1002/2013JD020122.

Arnone, E., and A. Hauchecorne (2012), Stratosphere NOy species measured by MIPAS and GOMOS onboard ENVISAT during 2002–2010: Influence of plasma processes onto the observed distribution and variability, *Space Sci. Rev.*, *168*(1-4), 315–332, doi:10.1007/s11214-011-9861-1.

Arnone, E., E. Castelli, E. Papandrea, M. Carlotti, and B. M. Dinelli (2012), Extreme ozone depletion in the 2010–2011 Arctic winter stratosphere as observed by MIPAS/ENVISAT using a 2-D tomographic approach, *Atmos. Chem. Phys.*, *12*(19), 9149–9165, doi:10.5194/acp-12-9149-2012.

Bardeen, C. G., O. B. Toon, E. J. Jensen, D. R. Marsh, and V. L. Harvey (2008), Numerical simulations of the three-dimensional distribution of meteoric dust in the mesosphere and upper stratosphere, *J. Geophys. Res.*, *113*, D17202, doi:10.1029/2007JD009515.

Barkstrom, B. R. (1978), Some effects of 8–12 μm radiant energy transfer on the mass and heat budgets of cloud droplets, *J. Atmos. Sci.*, *35*(4), 665–673, doi:10.1175/1520-0469(1978)035<0665:SEORET>2.0.CO;2.

Baumgardner, D., J. E. Dye, B. W. Gandrud, and R. G. Knollenberg (1992), Interpretation of measurements made by the forward scattering spectrometer probe (FSSP-300) during the Airborne Arctic Stratospheric Expedition, *J. Geophys. Res.*, *97*(D8), 8035–8046, doi:10.1029/91JD02728.

Bernath, P. (2006), Atmospheric chemistry experiment (ACE): Analytical chemistry from orbit, *TrAC Trends Anal. Chem.*, *25*(7), 647–654, doi:10.1016/j.trac.2006.05.001.

Bertram, A. K., and J. J. Sloan (1998), The nucleation rate constants and freezing mechanism of nitric acid trihydrate aerosol under stratospheric conditions, *J. Geophys. Res.*, *103*(D11), 13,261–13,265, doi:10.1029/98JD00921.

Bertram, A. K., D. D. Patterson, and J. J. Sloan (1996), Mechanisms and temperatures for the freezing of sulfuric acid aerosols measured by FTIR extinction spectroscopy, *J. Phys. Chem.*, *100*(6), 2376–2383, doi:10.1021/jp952551v.

Biermann, U. M., J. N. Crowley, T. Huthwelker, G. K. Moortgat, P. J. Crutzen, and T. Peter (1998), FTIR studies on lifetime prolongation of stratospheric ice particles due to NAT coating, *Geophys. Res. Lett.*, *25*(21), 3939–3942, doi:10.1029/1998GL900040.

Bohren, C. F., and D. R. Huffman (1983), *Absorption and Scattering of Light by Small Particles*, vol. 1, 541 pp., Wiley-Interscience, N. Y.

Bovensmann, H., J. P. Burrows, M. Buchwitz, J. Frerick, S. Noël, V. V. Rozanov, K. V. Chance, and A. P. H. Goede (1999), SCIAMACHY: Mission objectives and measurement modes, *J. Atmos. Sci.*, *56*(2), 127–150, doi:10.1175/1520-0469(1999)056<0127:SMOAMM>2.0.CO;2.

Brakebusch, M. (2013), *Chemistry Climate Model Simulations of Polar Stratospheric Ozone*, 150 pp., Univ. of Colo. at Boulder, Ann Arbor, Mich.

Brakebusch, M., C. E. Randall, D. E. Kinnison, S. Tilmes, M. L. Santee, and G. L. Manney (2013), Evaluation of Whole Atmosphere Community Climate Model simulations of ozone during Arctic winter 2004–2005, *J. Geophys. Res. Atmos.*, *118*, 2673–2688, doi:10.1002/jgrd.50226.

Brasseur, G. P., D. A. Hauglustaine, S. Walters, P. J. Rasch, J.-F. Müller, C. Granier, and X. X. Tie (1998), MOZART, a global chemical transport model for ozone and related chemical tracers: 1. Model description, *J. Geophys. Res.*, *103*(D21), 28,265–28,289, doi:10.1029/98JD02397.

Brooks, S. D., D. Baumgardner, B. Gandrud, J. E. Dye, M. J. Northway, D. W. Fahey, T. P. Bui, O. B. Toon, and M. A. Tolbert (2003), Measurements of large stratospheric particles in the Arctic polar vortex, *J. Geophys. Res.*, *108*(D20), 4652, doi:10.1029/2002JD003278.

Burrows, J. P., E. Hölzle, A. P. H. Goede, H. Visser, and W. Fricke (1995), SCIAMACHY—Scanning imaging absorption spectrometer for atmospheric chartography, *Acta Astronaut.*, *35*(7), 445–451, doi:10.1016/0094-5765(94)00278-T.

Carslaw, K. S., B. Luo, and T. Peter (1995), An analytic expression for the composition of aqueous HNO_3-H_2SO_4 stratospheric aerosols including gas phase removal of HNO3, *Geophys. Res. Lett.*, *22*(14), 1877–1880, doi:10.1029/95GL01668.

Carslaw, K. S., M. Wirth, A. Tsias, B. P. Luo, A. Dörnbrack, M. Leutbecher, H. Volkert, W. Renger, J. T. Bacmeister, and T. Peter (1998), Particle microphysics and chemistry in remotely observed mountain polar stratospheric clouds, *J. Geophys. Res.*, *103*(D5), 5785–5796, doi:10.1029/97JD03626.

Carslaw, K. S., J. A. Kettleborough, M. J. Northway, S. Davies, R.-S. Gao, D. W. Fahey, D. G. Baumgardner, M. P. Chipperfield, and A. Kleinböhl (2002), A vortex-scale simulation of the growth and sedimentation of large nitric acid hydrate particles, *J. Geophys. Res.*, *107*(D20), 8300, doi:10.1029/2001JD000467.

Chan, T., and M. Mozurkewich (2001), Measurement of the coagulation rate constant for sulfuric acid particles as a function of particle size using tandem differential mobility analysis, *J. Aerosol Sci.*, *32*(3), 321–339, doi:10.1016/S0021-8502(00)00081-1.

Cheng, Y.-S., H.-C. Yeh, and M. D. Allen (1988), Dynamic shape factor of a plate-like particle, *Aerosol Sci. Technol.*, *8*(2), 109–123, doi:10.1080/02786828808959176.

Crowley, J. N., M. Ammann, R. A. Cox, R. G. Hynes, M. E. Jenkin, A. Mellouki, M. J. Rossi, J. Troe, and T. J. Wallington (2010), Evaluated kinetic and photochemical data for atmospheric chemistry: Volume V—Heterogeneous reactions on solid substrates, *Atmos. Chem. Phys.*, *10*(18), 9059–9223, doi:10.5194/acp-10-9059-2010.

Curtius, J., et al. (2005), Observations of meteoric material and implications for aerosol nucleation in the winter Arctic lower stratosphere derived from in situ particle measurements, *Atmos. Chem. Phys.*, *5*(11), 3053–3069, doi:10.5194/acp-5-3053-2005.

Daerden, F., N. Larsen, S. Chabrillat, Q. Errera, S. Bonjean, D. Fonteyn, K. Hoppel, and M. Fromm (2007), A 3D-CTM with detailed online PSC-microphysics: Analysis of the Antarctic winter 2003 by comparison with satellite observations, *Atmos. Chem. Phys.*, *7*(7), 1755–1772, doi:10.5194/acp-7-1755-2007.

Deshler, T., and S. Oltmans (1998), Vertical profiles of volcanic aerosol and polar stratospheric clouds above Kiruna, Sweden: Winters 1993 and 1995, *J. Atmos. Chem.*, *30*(1), 11–23, doi:10.1023/A:1006023729315.

Deshler, T., et al. (2003a), Large nitric acid particles at the top of an Arctic stratospheric cloud, *J. Geophys. Res.*, *108*(D16), 4517, doi:10.1029/2003JD003479.

Deshler, T., M. E. Hervig, D. J. Hofmann, J. M. Rosen, and J. B. Liley (2003b), Thirty years of in situ stratospheric aerosol size distribution measurements from Laramie, Wyoming (41°N), using balloon-borne instruments, *J. Geophys. Res.*, *108*(D5), 4167, doi:10.1029/2002JD002514.

Dinelli, B. M., E. Arnone, G. Brizzi, M. Carlotti, E. Castelli, L. Magnani, E. Papandrea, M. Prevedelli, and M. Ridolfi (2010), The MIPAS2D database of MIPAS/ENVISAT measurements retrieved with a multi-target 2-dimensional tomographic approach, *Atmos. Meas. Tech.*, *3*(2), 355–374, doi:10.5194/amt-3-355-2010.

Disselkamp, R. S., S. E. Anthony, A. J. Prenni, T. B. Onasch, and M. A. Tolbert (1996), Crystallization kinetics of nitric acid dihydrate aerosols, *J. Phys. Chem.*, *100*(21), 9127–9137, doi:10.1021/jp953608g.

Dodion, J., et al. (2007), Cloud detection in the upper troposphere-lower stratosphere region via ACE imagers: A qualitative study, *J. Geophys. Res.*, *112*, D03208, doi:10.1029/2006JD007160.

Draine, B. T., and P. J. Flatau (1994), Discrete-dipole approximation for scattering calculations, *J. Opt. Soc. Am. A Opt. Image Sci.*, *11*(4), 1491–1499, doi:10.1364/JOSAA.11.001491.

Drdla, K., and R. Müller (2012), Temperature thresholds for chlorine activation and ozone loss in the polar stratosphere, *Ann. Geophys.*, *30*, 1055–1073, doi:10.5194/angeo-30-1055-2012.

Dunkerton, T. J., and D. P. Delisi (1986), Evolution of potential vorticity in the winter stratosphere of January-February 1979, *J. Geophys. Res.*, *91*(D1), 1199–1208, doi:10.1029/JD091iD01p01199.

Dye, J. E., B. W. Gandrud, D. Baumgardner, L. Sanford, and G. V. Ferry (1990), A survey of particle measurements in the Arctic from the Forward Scattering Spectrometer Probe MODEL 300, *Geophys. Res. Lett.*, *17*(4), 409–412, doi:10.1029/GL017i004p00409.

Dye, J. E., D. Baumgardner, B. W. Gandrud, S. R. Kawa, K. K. Kelly, M. Loewenstein, G. V. Ferry, K. R. Chan, and B. L. Gary (1992), Particle size distributions in Arctic polar stratospheric clouds, growth and freezing of sulfuric acid droplets, and implications for cloud formation, *J. Geophys. Res.*, *97*(D8), 8015–8034, doi:10.1029/91JD02740.

Emmons, L. K., et al. (2010), Description and evaluation of the Model for Ozone and Related chemical Tracers, version 4 (MOZART-4), *Geosci. Model Dev.*, *3*(1), 43–67, doi:10.5194/gmd-3-43-2010.

Engel, I., B. P. Luo, M. C. Pitts, L. R. Poole, C. R. Hoyle, J.-U. Grooß, A. Dörnbrack, and T. Peter (2013), Heterogeneous formation of polar stratospheric clouds—Part 2: Nucleation of ice on synoptic scales, *Atmos. Chem. Phys.*, *13*(21), 10,769–10,785, doi:10.5194/acp-13-10769-2013.

English, J. M., O. B. Toon, M. J. Mills, and F. Yu (2011), Microphysical simulations of new particle formation in the upper troposphere and lower stratosphere, *Atmos. Chem. Phys.*, *11*(17), 9303–9322, doi:10.5194/acp-11-9303-2011.

Eyring, V., M. P. Chipperfield, M. A. Giorgetta, D. E. Kinnison, E. Manzini, K. Matthes, P. A. Newman, S. Pawson, T. G. Shepherd, and D. W. Waugh (2008), Overview of the new CCMVal reference and sensitivity simulations in support of upcoming ozone and climate assessments and the planned SPARC CCMVal report, *SPARC Newsl.*, *30*, 20–26.

Fahey, D. W., et al. (2001), The detection of large HNO3-containing particles in the winter Arctic stratosphere., *Science*, *291*(5506), 1026–1031, doi:10.1126/science.1057265.
Fischer, H., et al. (2008), MIPAS: An instrument for atmospheric and climate research, *Atmos. Chem. Phys.*, *8*(8), 2151–2188, doi:10.5194/acp-8-2151-2008.
Fortin, T. J., K. Drdla, L. T. Iraci, and M. A. Tolbert (2003), Ice condensation on sulfuric acid tetrahydrate: Implications for polar stratospheric ice clouds, *Atmos. Chem. Phys.*, *3*(4), 987–997, doi:10.5194/acp-3-987-2003.
Fuks, N. A. (1964), *The Mechanics of Aerosols*, Pergamon, N. Y.
Garcia, R. R., D. R. Marsh, D. E. Kinnison, B. A. Boville, and F. Sassi (2007), Simulation of secular trends in the middle atmosphere, 1950–2003, *J. Geophys. Res.*, *112*, D09301, doi:10.1029/2006JD007485.
Grooß, J.-U., et al. (2014), Nitric acid trihydrate nucleation and denitrification in the Arctic stratosphere, *Atmos. Chem. Phys.*, *14*(2), 1055–1073, doi:10.5194/acp-14-1055-2014.
Hamill, P., R. P. Turco, C. S. Kiang, O. B. Toon, and R. C. Whitten (1982), An analysis of various nucleation mechanisms for sulfate particles in the stratosphere, *J. Aerosol Sci.*, *13*(6), 561–585, doi:10.1016/0021-8502(82)90021-0.
Hanson, D., and K. Mauersberger (1988), Laboratory studies of the nitric acid trihydrate: Implications for the south polar stratosphere, *Geophys. Res. Lett.*, *15*, 855–858, doi:10.1029/GL015i008p00855.
Hanson, D. R., A. R. Ravishankara, and S. Solomon (1994), Heterogeneous reactions in sulfuric acid aerosols: A framework for model calculations, *J. Geophys. Res.*, *99*(D2), 3615–3629, doi:10.1029/93JD02932.
Hauglustaine, D. A., G. P. Brasseur, S. Walters, P. J. Rasch, J.-F. Müller, L. K. Emmons, and M. A. Carroll (1998), MOZART, a global chemical transport model for ozone and related chemical tracers: 2. Model results and evaluation, *J. Geophys. Res.*, *103*(D21), 28,291–28,335, doi:10.1029/98JD02398.
Hommel, R., et al. (2014), Chemical ozone loss and ozone mini-hole event during the Arctic winter 2010/2011 as observed by SCIAMACHY and GOME-2, *Atmos. Chem. Phys.*, *14*(7), 3247–3276, doi:10.5194/acp-14-3247-2014.
Höpfner, M., et al. (2006), Spectroscopic evidence for NAT, STS, and ice in MIPAS infrared limb emission measurements of polar stratospheric clouds, *Atmos. Chem. Phys.*, *6*(5), 1201–1219, doi:10.5194/acp-6-1201-2006.
Horowitz, L. W., et al. (2003), A global simulation of tropospheric ozone and related tracers: Description and evaluation of MOZART, version 2, *J. Geophys. Res.*, *108*(D24), 4784, doi:10.1029/2002JD002853.
Hoyle, C. R., I. Engel, B. P. Luo, M. C. Pitts, L. R. Poole, J.-U. Grooß, and T. Peter (2013), Heterogeneous formation of polar stratospheric clouds—Part 1: Nucleation of nitric acid trihydrate (NAT), *Atmos. Chem. Phys.*, *13*(18), 9577–9595, doi:10.5194/acp-13-9577-2013.
Iraci, L. T., A. M. Middlebrook, and M. A. Tolbert (1995), Laboratory studies of the formation of polar stratospheric clouds: Nitric acid condensation on thin sulfuric acid films, *J. Geophys. Res.*, *100*(D10), 20,969–20,977, doi:10.1029/95JD02267.
Jacobson, M. Z., R. P. Turco, E. J. Jensen, and O. B. Toon (1994), Modeling coagulation among particles of different composition and size, *Atmos. Environ.*, *28*(7), 1327–1338, doi:10.1016/1352-2310(94)90280-1.
Kawa, S. R., et al. (1997), Activation of chlorine in sulfate aerosol as inferred from aircraft observations, *J. Geophys. Res.*, *102*(D3), 3921–3933, doi:10.1029/96JD01992.
Kelly, K. K., et al. (1989), Dehydration in the lower Antarctic stratosphere during late winter and early spring, 1987, *J. Geophys. Res.*, *94*(D9), 11,317–11,357, doi:10.1029/JD094iD09p11317.
Kinnison, D. E., et al. (2007), Sensitivity of chemical tracers to meteorological parameters in the MOZART-3 chemical transport model, *J. Geophys. Res.*, *112*, D20302, doi:10.1029/2006JD007879.
Knopf, D. A., T. Koop, B. P. Luo, U. G. Weers, and T. Peter (2002), Homogeneous nucleation of NAD and NAT in liquid stratospheric aerosols: Insufficient to explain denitrification, *Atmos. Chem. Phys.*, *2*(3), 207–214, doi:10.5194/acp-2-207-2002.
Koop, T., and K. S. Carslaw (1996), Melting of $H_2SO_4{\cdot}4H_2O$ Particles upon Cooling: Implications for Polar Stratospheric Clouds, *Science*, *272*(5268), 1638–1641, doi:10.1126/science.272.5268.1638.
Koop, T., U. M. Biermann, W. Raber, B. P. Luo, P. J. Crutzen, and T. Peter (1995), Do stratospheric aerosol droplets freeze above the ice frost point?, *Geophys. Res. Lett.*, *22*(8), 917–920, doi:10.1029/95GL00814.
Koop, T., B. Luo, U. M. Biermann, P. J. Crutzen, and T. Peter (1997), Freezing of $HNO_3/H_2SO_4/H_2O$ solutions at stratospheric temperatures: Nucleation statistics and experiments, *J. Phys. Chem. A*, *101*(6), 1117–1133, doi:10.1021/jp9626531.
Koop, T., B. Luo, A. Tsias, and T. Peter (2000), Water activity as the determinant for homogeneous ice nucleation in aqueous solutions, *Nature*, *406*(6796), 611–614.
Kühl, S., A. Dörnbrack, W. Wilms-Grabe, B.-M. Sinnhuber, U. Platt, and T. Wagner (2004), Observational evidence of rapid chlorine activation by mountain waves above northern Scandinavia, *J. Geophys. Res.*, *109*, D22309, doi:10.1029/2004JD004797.
Kulmala, M., and A. Laaksonen (1990), Binary nucleation of water–sulfuric acid system: Comparison of classical theories with different H_2SO_4 saturation vapor pressures, *J. Chem. Phys.*, *93*(1), 696, doi:10.1063/1.459519.
Lamarque, J.-F., et al. (2012), CAM-chem: Description and evaluation of interactive atmospheric chemistry in the Community Earth System Model, *Geosci. Model Dev.*, *5*(2), 369–411, doi:10.5194/gmd-5-369-2012.
Lambert, A., M. L. Santee, D. L. Wu, and J. H. Chae (2012), A-train CALIOP and MLS observations of early winter Antarctic polar stratospheric clouds and nitric acid in 2008, *Atmos. Chem. Phys.*, *12*(6), 2899–2931.
Larsen, N. (2000), Polar stratospheric clouds: Microphysical and optical models, Danish Meteorological Institute, Report 00–06, Copenhagen.
Le Clair, B. P., A. E. Hamielec, and H. R. Pruppacher (1970), A Numerical study of the drag on a sphere at low and intermediate Reynolds numbers, *J. Atmos. Sci.*, *27*(2), 308–315, doi:10.1175/1520-0469(1970)027<0308:ANSOTD>2.0.CO;2.
Lin, S.-J., and R. B. Rood (1996), Multidimensional flux-form semi-Lagrangian transport schemes, *Mon. Weather Rev.*, *124*(9), 2046–2070, doi:10.1175/1520-0493(1996)124<2046:MFFSLT>2.0.CO;2.
Lin, S.-J., and R. B. Rood (1997), An explicit flux-form semi-lagrangian shallow-water model on the sphere, *Q. J. R. Meteorol. Soc.*, *123*(544), 2477–2498, doi:10.1002/qj.49712354416.
Livesey, N. J., et al. (2011), Version 3.3 Level 2 data quality and description document, Jet Propulsion Laboratory California Institute of Technology, Pasadena, Calif.
Lowe, D., and A. R. MacKenzie (2008), Polar stratospheric cloud microphysics and chemistry, *J. Atmos. Sol. Terr. Phys.*, *70*(1), 13–40, doi:10.1016/j.jastp.2007.09.011.
Luo, B., K. S. Carslaw, T. Peter, and S. L. Clegg (1995), Vapour pressures of $H_2SO_4/HNO_3/HCl/HBr/H_2O$ solutions to low stratospheric temperatures, *Geophys. Res. Lett.*, *22*(3), 247–250, doi:10.1029/94GL02988.
Luo, B., U. K. Krieger, and T. Peter (1996), Densities and refractive indices of $H_2SO_4/HNO_3/H_2O$ solutions to stratospheric temperatures, *Geophys. Res. Lett.*, *23*(25), 3707–3710, doi:10.1029/96GL03581.

Luo, B. P., C. Voigt, S. Fueglistaler, and T. Peter (2003), Extreme NAT supersaturations in mountain wave ice PSCs: A clue to NAT formation, *J. Geophys. Res.*, *108*(D15), 4441, doi:10.1029/2002JD003104.
MacKenzie, A. R., M. Kulmala, A. Laaksonen, and T. Vesala (1995), On the theories of type 1 polar stratospheric cloud formation, *J. Geophys. Res.*, *100*(D6), 11,275–11,288, doi:10.1029/95JD00699.
Manney, G. L., R. W. Zurek, A. O'Neill, and R. Swinbank (1994), On the motion of air through the stratospheric polar vortex, *J. Atmos. Sci.*, *51*(20), 2973–2994, doi:10.1175/1520-0469(1994)051<2973:OTMOAT>2.0.CO;2.
Manney, G. L., et al. (2011), Unprecedented Arctic ozone loss in 2011, *Nature*, *478*(7370), 469–475, doi:10.1038/nature10556.
Marsh, D. R., M. J. Mills, D. E. Kinnison, J.-F. Lamarque, N. Calvo, and L. M. Polvani (2013), Climate change from 1850 to 2005 simulated in CESM1(WACCM), *J. Clim.*, *26*(19), 7372–7391, doi:10.1175/JCLI-D-12-00558.1.
Martin, E., C. George, and P. Mirabel (2000), Densities and surface tensions of $H_2SO_4/HNO_3/H_2O$ solutions, *Geophys. Res. Lett.*, *27*(2), 197–200, doi:10.1029/1999GL010892.
Matsuno, T. (1971), A dynamical model of the stratospheric sudden warming, *J. Atmos. Sci.*, *28*(8), 1479–1494, doi:10.1175/1520-0469(1971)028<1479:ADMOTS>2.0.CO;2.
Middlebrook, A. M., L. T. Iraci, L. S. McNeill, B. G. Koehler, M. A. Wilson, O. W. Saastad, M. A. Tolbert, and D. R. Hanson (1993), Fourier transform-infrared studies of thin H_2SO_4/H_2O films: Formation, water uptake, and solid-liquid phase changes, *J. Geophys. Res.*, *98*(D11), 20,473–20,481, doi:10.1029/93JD02454.
Middlebrook, A. M., M. A. Tolbert, and K. Drdla (1996), Evaporation studies of model polar stratospheric cloud films, *Geophys. Res. Lett.*, *23*(16), 2145–2148, doi:10.1029/96GL01962.
Molina, L. T., and M. J. Molina (1987), Production of chlorine oxide (Cl_2O_2) from the self-reaction of the chlorine oxide (ClO) radical, *J. Phys. Chem.*, *91*(2), 433–436, doi:10.1021/j100286a035.
Molleker, S., et al. (2014), Microphysical properties of synoptic scale polar stratospheric clouds: In situ measurements of unexpectedly large HNO_3 containing particles in the Arctic vortex, *Atmos. Chem. Phys.*, *14*, 10,785–10,801, doi:10.5194/acp-14-10785-2014.
Murphy, D. M., D. J. Cziczo, P. K. Hudson, and D. S. Thomson (2007), Carbonaceous material in aerosol particles in the lower stratosphere and tropopause region, *J. Geophys. Res.*, *112*, D04203, doi:10.1029/2006JD007297.
Neely, R. R., J. M. English, O. B. Toon, S. Solomon, M. Mills, and J. P. Thayer (2011), Implications of extinction due to meteoritic smoke in the upper stratosphere, *Geophys. Res. Lett.*, *38*, L24808, doi:10.1029/2011GL049865.
Ovarlez, J., and H. Ovarlez (1994), Stratospheric water vapor content evolution during EASOE, *Geophys. Res. Lett.*, *21*(13), 1235–1238, doi:10.1029/93GL02438.
Peter, T., R. Müller, P. J. Crutzen, and T. Deshler (1994), The lifetime of leewave-induced ice particles in the Arctic stratosphere: II. Stabilization due to NAT-coating, *Geophys. Res. Lett.*, *21*(13), 1331–1334, doi:10.1029/93GL03019.
Pitts, M. C., L. W. Thomason, L. R. Poole, and D. M. Winker (2007), Characterization of Polar Stratospheric Clouds with spaceborne lidar: CALIPSO and the 2006 Antarctic season, *Atmos. Chem. Phys.*, *7*(19), 5207–5228, doi:10.5194/acp-7-5207-2007.
Pitts, M. C., L. R. Poole, and L. W. Thomason (2009), CALIPSO polar stratospheric cloud observations: Second-generation detection algorithm and composition discrimination, *Atmos. Chem. Phys.*, *9*(19), 7577–7589, doi:10.5194/acp-9-7577-2009.
Pitts, M. C., L. R. Poole, A. Dörnbrack, and L. W. Thomason (2011), The 2009–2010 Arctic polar stratospheric cloud season: A CALIPSO perspective, *Atmos. Chem. Phys.*, *11*(5), 2161–2177, doi:10.5194/acp-11-2161-2011.
Pitts, M. C., L. R. Poole, A. Lambert, and L. W. Thomason (2013), An assessment of CALIOP polar stratospheric cloud composition classification, *Atmos. Chem. Phys.*, *13*(6), 2975–2988, doi:10.5194/acp-13-2975-2013.
Pruppacher, H. R., and J. D. Klett (1997), *Microphysics of Clouds and Precipitation*, 2nd ed., Kluwer Acad., Dordrecht, Netherlands.
Ramaswamy, V., and A. Detwiler (1986), Interdependence of radiation and microphysics in cirrus clouds, *J. Atmos. Sci.*, *43*(21), 2289–2301, doi:10.1175/1520-0469(1986)043<2289:IORAMI>2.0.CO;2.
Reinecker, M. M., et al. (2008), The GEOS-5 data assimilation system—Documentation of versions 5.0.1 and 5.1.0, NASA Tech Rep. TM-2007-104606, vol. 27, 92 pp.
Rieder, H. E., L. M. Polvani, and S. Solomon (2014), Distinguishing the impacts of ozone-depleting substances and well-mixed greenhouse gases on Arctic stratospheric ozone and temperature trends, *Geophys. Res. Lett.*, *41*, 2652–2660, doi:10.1002/2014GL059367.
Salcedo, D., L. T. Molina, and M. J. Molina (2000), Homogeneous freezing of concentrated aqueous nitric acid solutions at polar stratospheric temperatures, *J. Phys. Chem. A*, *105*(9), 1433–1439, doi:10.1021/jp001639s.
Schoeberl, M. R. (2007), The EOS Aura Mission, in *Observing Systems for Atmospheric Composition*, pp. 64–70, Springer, N. Y.
Schoeberl, M. R., and A. E. Dessler (2011), Dehydration of the stratosphere, *Atmos. Chem. Phys.*, *11*(16), 8433–8446, doi:10.5194/acp-11-8433-2011.
Schreiner, J., C. Voigt, P. Zink, A. Kohlmann, D. Knopf, C. Weisser, P. Budz, and K. Mauersberger (2002), A mass spectrometer system for analysis of polar stratospheric aerosols, *Rev. Sci. Instrum.*, *73*(2), 446–452.
Schwartz, M. J., et al. (2008), Validation of the Aura Microwave Limb Sounder temperature and geopotential height measurements, *J. Geophys. Res.*, *113*, D15S11, doi:10.1029/2007JD008783.
Shi, Q., J. T. Jayne, C. E. Kolb, D. R. Worsnop, and P. Davidovits (2001), Kinetic model for reaction of $ClONO_2$ with H_2O and HCl and HOCl with HCl in sulfuric acid solutions, *J. Geophys. Res.*, *106*(D20), 24,259–24,274, doi:10.1029/2000JD000181.
Sinnhuber, B.-M., G. Stiller, R. Ruhnke, T. von Clarmann, S. Kellmann, and J. Aschmann (2011), Arctic winter 2010/2011 at the brink of an ozone hole, *Geophys. Res. Lett.*, *38*, L24814, doi:10.1029/2011GL049784.
Solomon, S., R. R. Garcia, F. S. Rowland, and D. J. Wuebbles (1986), On the depletion of Antarctic ozone, *Nature*, *321*(6072), 755–758.
Tabazadeh, A., R. P. Turco, K. Drdla, M. Z. Jacobson, and O. B. Toon (1994), A study of type I polar stratospheric cloud formation, *Geophys. Res. Lett.*, *21*(15), 1619–1622, doi:10.1029/94GL01368.
Tabazadeh, A., O. B. Toon, S. L. Clegg, and P. Hamill (1997), A new parameterization of H_2SO4/H_2O aerosol composition: Atmospheric implications, *Geophys. Res. Lett.*, *24*(15), 1931–1934, doi:10.1029/97GL01879.
Tabazadeh, A., Y. S. Djikaev, P. Hamill, and H. Reiss (2002), Laboratory evidence for surface nucleation of solid polar stratospheric cloud particles, *J. Phys. Chem. A*, *106*(43), 10,238–10,246, doi:10.1021/jp021045k.
Taesler, I., R. G. Delaplane, and I. Olovsson (1975), Hydrogen bond studies. XCIV. Diaquaoxonium ion in nitric acid trihydrate, *Acta Crystallogr., Sect. B Struct. Crystallogr. Cryst. Chem.*, *31*(5), 1489–1492.
Tang, M. J., R. A. Cox, and M. Kalberer (2014), Compilation and evaluation of gas-phase diffusion coefficients of inorganic reactive trace gases in the atmosphere, *Atmos. Chem. Phys. Discuss.*, *14*(10), 15,645–15,682, doi:10.5194/acpd-14-15645-2014.
Toon, O. B., P. Hamill, R. P. Turco, and J. Pinto (1986), Condensation of HNO_3 and HCl in the winter polar stratospheres, *Geophys. Res. Lett.*, *13*(12), 1284–1287, doi:10.1029/GL013i012p01284.

Toon, O. B., R. P. Turco, D. Westphal, R. Malone, and M. Liu (1988), A multidimensional model for aerosols: Description of computational analogs, *J. Atmos. Sci.*, *45*(15), 2123–2144, doi:10.1175/1520-0469(1988)045<2123:AMMFAD>2.0.CO;2.

Toon, O. B., R. P. Turco, J. Jordan, J. Goodman, and G. Ferry (1989), Physical processes in polar stratospheric ice clouds, *J. Geophys. Res.*, *94*(D9), 11,359–11,380, doi:10.1029/JD094iD09p11359.

Toon, O. B., R. P. Turco, and P. Hamill (1990), Denitrification mechanisms in the polar stratospheres, *Geophys. Res. Lett.*, *17*(4), 445–448, doi:10.1029/GL017i004p00445.

Toon, O. B., A. Tabazadeh, E. V. Browell, and J. Jordan (2000), Analysis of lidar observations of Arctic polar stratospheric clouds during January 1989, *J. Geophys. Res. Atmos.*, *105*(D16), 20,589–20,615, doi:10.1029/2000JD900144.

Tsias, A., A. J. Prenni, K. S. Carslaw, T. P. Onasch, B. P. Luo, M. A. Tolbert, and T. Peter (1997), Freezing of polar stratospheric clouds in orographically induced strong warming events, *Geophys. Res. Lett.*, *24*(18), 2303–2306, doi:10.1029/97GL02181.

Turco, R. P., P. Hamill, O. B. Toon, R. C. Whitten, and C. S. Kiang (1979), A one-dimensional model describing aerosol formation and evolution in the stratosphere: I. Physical processes and mathematical analogs, *J. Atmos. Sci.*, *36*(4), 699–717, doi:10.1175/1520-0469(1979)036<0699:AODMDA>2.0.CO;2.

Voigt, C., et al. (2005), Nitric Acid Trihydrate (NAT) formation at low NAT supersaturation in Polar Stratospheric Clouds (PSCs), *Atmos. Chem. Phys.*, *5*(5), 1371–1380, doi:10.5194/acp-5-1371-2005.

Von Hobe, M., et al. (2013), Reconciliation of essential process parameters for an enhanced predictability of Arctic stratospheric ozone loss and its climate interactions (RECONCILE): Activities and results, *Atmos. Chem. Phys.*, *13*(18), 9233–9268, doi:10.5194/acp-13-9233-2013.

Von Savigny, C., E. P. Ulasi, K.-U. Eichmann, H. Bovensmann, and J. P. Burrows (2005), Detection and mapping of polar stratospheric clouds using limb scattering observations, *Atmos. Chem. Phys.*, *5*(11), 3071–3079, doi:10.5194/acp-5-3071-2005.

Waibel, A. E., T. Peter, K. S. Carslaw, H. Oelhaf, G. Wetzel, P. J. Crutzen, U. Pöschl, A. Tsias, E. Reimer, and H. Fischer (1999), Arctic ozone loss due to denitrification, *Science*, *283* (5410), 2064–2069, doi:10.1126/science.283.5410.2064.

Waters, J. W., et al. (1999), The UARS and EOS Microwave Limb Sounder (MLS) experiments, *J. Atmos. Sci.*, *56*(2), 194–218, doi:10.1175/1520-0469(1999)056<0194:TUAEML>2.0.CO;2.

Wegner, T., J.-U. Grooß, M. von Hobe, F. Stroh, O. Sumińska-Ebersoldt, C. M. Volk, E. Hösen, V. Mitev, G. Shur, and R. Müller (2012), Heterogeneous chlorine activation on stratospheric aerosols and clouds in the Arctic polar vortex, *Atmos. Chem. Phys.*, *12*(22), 11,095–11,106, doi:10.5194/acp-12-11095-2012.

Wegner, T., D. E. Kinnison, R. R. Garcia, and S. Solomon (2013), Simulation of polar stratospheric clouds in the specified dynamics version of the whole atmosphere community climate model, *J. Geophys. Res. Atmos.*, *118*, 4991–5002, doi:10.1002/jgrd.50415.

Weigel, R., C. M. Volk, K. Kandler, E. Hösen, G. Günther, B. Vogel, J.-U. Grooß, S. Khaykin, G. V. Belyaev, and S. Borrmann (2014), Enhancements of the refractory submicron aerosol fraction in the Arctic polar vortex: Feature or exception?, *Atmos. Chem. Phys.*, *14*(22), 12,319–12,342, doi:10.5194/acp-14-12319-2014.

Weisser, C., K. Mauersberger, J. Schreiner, N. Larsen, F. Cairo, A. Adriani, J. Ovarlez, and T. Deshler (2006), Composition analysis of liquid particles in the Arctic stratosphere under synoptic conditions, *Atmos. Chem. Phys.*, *6*(3), 689–696, doi:10.5194/acp-6-689-2006.

Winker, D. M., W. H. Hunt, and M. J. McGill (2007), Initial performance assessment of CALIOP, *Geophys. Res. Lett.*, *34*, L19803, doi:10.1029/2007GL030135.

Wirth, M., A. Tsias, A. Dörnbrack, V. Weiß, K. S. Carslaw, M. Leutbecher, W. Renger, H. Volkert, and T. Peter (1999), Model-guided Lagrangian observation and simulation of mountain polar stratospheric clouds, *J. Geophys. Res.*, *104*(D19), 23,971–23,981, doi:10.1029/1998JD100095.

Woiwode, W., et al. (2014), Denitrification by large NAT particles: The impact of reduced settling velocities and hints on particle characteristics, *Atmos. Chem. Phys.*, *14*(20), 11,525–11,544, doi:10.5194/acp-14-11525-2014.

Zasetsky, A. Y., K. Gilbert, I. Galkina, S. McLeod, and J. J. Sloan (2007), Properties of polar stratospheric clouds obtained by combined ACE-FTS and ACE-Imager extinction measurements, *Atmos. Chem. Phys. Discuss.*, *7*(5), 13,271–13,290, doi:10.5194/acpd-7-13271-2007.

Zhang, R., P. J. Wooldridge, and M. J. Molina (1993), Vapor pressure measurements for the $H_2SO_4/HNO_3/H_2O$ and $H_2SO_4/HCl/H_2O$ systems: Incorporation of stratospheric acids into background sulfate aerosols, *J. Phys. Chem.*, *97*(32), 8541–8548.

Zondlo, M. A., P. K. Hudson, A. J. Prenni, and M. A. Tolbert (2000), Chemistry and microphysics of polar stratospheric clouds and cirrus clouds, *Annu. Rev. Phys. Chem.*, *51*(1), 473–499, doi:10.1146/annurev.physchem.51.1.473.